Density of states method for symplectic gauge theories at finite temperature

Ed Bennett[1,*] Biagio Lucini[1,2,3,†] David Mason[4,2,5,‡] Maurizio Piai,[4,§]
Enrico Rinaldi[6,‖] and Davide Vadacchino[7,¶]

[1]*Swansea Academy of Advanced Computing, Swansea University,
Fabian Way, SA1 8EN, Swansea, Wales, United Kingdom*
[2]*Department of Mathematics, Faculty of Science and Engineering, Swansea University,
Fabian Way, SA1 8EN Swansea, Wales, United Kingdom*
[3]*School of Mathematical Sciences, Queen Mary University of London,
Mile End Road, London, E1 4NS, United Kingdom*
[4]*Department of Physics, Faculty of Science and Engineering, Swansea University,
Singleton Park, SA2 8PP, Swansea, Wales, United Kingdom*
[5]*Jülich Supercomputing Centre, Forschungszentrum Jülich, D-52425 Jülich, Germany*
[6]*Interdisciplinary Theoretical and Mathematical Science Program, RIKEN (iTHEMS),
2-1 Hirosawa, Wako, Saitama, 351-0198, Japan*
[7]*Centre for Mathematical Sciences, University of Plymouth, Plymouth, PL4 8AA, United Kingdom*

We study the finite-temperature behavior of the $Sp(4)$ Yang-Mills lattice theory in four dimensions, by applying the logarithmic linear relaxation algorithm. We demonstrate the presence of coexisting (metastable) phases, when the system is in the proximity of the transition. We measure observables such as the free energy, the expectation value of the plaquette operator and of the Polyakov loop, as well as the specific heat, and the Binder cumulant. We use these results to obtain a high-precision measurement of the critical coupling at the confinement-deconfinement transition, and assess its systematic uncertainty, for one value of the lattice extent in the time direction. Furthermore, we perform an extensive study of the finite-volume behavior of the lattice system, by repeating the measurements for fixed lattice time extent, while increasing the spatial size of the lattice. We hence characterize the first-order transition on the lattice and present the first results in the literature on this theory for the infinite volume extrapolation of lattice quantities related to latent heat and interface tension. Gauge theories with $Sp(4)$ group have been proposed as new dark sectors to provide a fundamental origin for the current phenomenological evidence of dark matter. A phase transition at high temperature, in such a new dark sector, occurring in the early Universe, might have left a relic stochastic background of gravitational waves. Our results represent a milestone toward establishing whether such a new physics signal is detectable in future experiments, as they enter the calculation of the parameters, α and β, controlling the power spectrum of gravitational waves. We also outline the process needed in the continuum extrapolation of our measurements and test its feasibility on one additional choice of temporal extent of the lattice.

*Contact author: e.j.bennett@swansea.ac.uk
†Contact author: b.lucini@swansea.ac.uk, b.lucini@qmul.ac.uk
‡Contact author: 2036508@Swansea.ac.uk, d.mason@fz-juelich.de
§Contact author: m.piai@swansea.ac.uk
‖Contact author: erinaldi.work@gmail.com
¶Contact author: davide.vadacchino@plymouth.ac.uk

I. INTRODUCTION

First-order phase transitions play a central role in our understanding of fundamental physics. They are particularly important in the context of the thermal history of the early Universe, and its relation to extensions of the Standard Model of particle physics. Nucleation and expansion of bubbles that result from first-order transitions have striking implications. They can provide the out-of-equilibrium condition satisfying one of the three requirements identified by Sakharov [1] to explain, via baryogenesis, the matter-antimatter asymmetry in the observable universe. Furthermore, bubble dynamics triggered by first-order phase transitions may lead to a relic

stochastic background of gravitational waves [2–7], which is testable in future experiments [8–25]—see also Ref. [26].

The thermal history of the Standard Model of particle physics proceeds via two smooth crossovers. Lattice simulations indicate that in quantum chromodynamics (QCD), with physical quark masses, deconfinement happens via a crossover [27]. The electroweak transition, in which the $SU(2)_L \times U(1)_Y$ gauge symmetry of the Standard Model breaks to the $U(1)$ of quantum electrodynamics (QED), has also been shown to be a crossover, by a combination of perturbative and nonperturbative results [28–34]—see Refs. [35,36] for reviews, and also Ref. [37] for a recent nonperturbative update. This finding is particularly disappointing, as it leads to the failure, within the Standard Model, of electroweak baryogenesis.

The past two decades saw the development of a whole branch of literature on new dark sectors—see for instance Refs. [38–44]. New matter fields carrying new strongly coupled interactions are postulated to exist, with only feeble couplings to the Standard Model, which allow such a dark sector and its particle content to have escaped experimental detection. In combination with the growing body of experimental evidence of dark matter (see the review in Ref. [45], and references therein), this has led to the formulation of a plethora of models realising this scenario. Depending on the details of the mechanism implemented, they may be referred to as composite dark matter models, such as those in Refs. [46–56], or strongly interacting massive particle (SIMP) models, such as those in Refs. [57–65]—see also the literature on dark $Sp(4)$ gauge theories [66–68], or the recent proposals in Refs. [69,70], and references therein, or stealth dark matter models [71,72], or dark baryon models [73].

If any such new, strongly coupled, dark sectors play a role in the early Universe, then it is of central importance to establish whether their finite-temperature dynamics leads to a first-order phase transition and furthermore to achieve a precise characterization of the physics in proximity of such a transition. By doing so, one can, in principle, determine those parameters that enter the calculation of the power spectrum of the relic stochastic background of gravitational waves. Borrowing notation from Ref. [24], the two prominent example are α and β/H_*, that are related to latent heat and bubble nucleation rate, respectively.[1] (They are used as input values in numerical packages such as PTPlot [24].) The highly challenging goal of measuring these parameters in strongly coupled theories is currently being pursued via several complementary investigation strategies—see the discussions in Ref. [75], and in Refs. [76–80]. Lattice numerical results can be supplemented by effective tools as the Polyakov-loop [81–89] or matrix models [90–98].

The finite-temperature behavior of lattice gauge theories is the subject of intense scrutiny. For a review of the current status of $SU(3)$ gauge theories, see the discussion in Ref. [99] and the review [100] (as well as Refs. [101,102]), Refs. [103–115] for pure gauge, and Refs. [116–121] for heavy quarks; for theories with other gauge groups, see for instance Refs. [122–127] for $SU(N)$, Refs. [128–131] for G_2, Refs. [71,72,132] for stealth dark matter with $SU(4)$ gauge group, and Ref. [133] for pioneering work on $Sp(2N)$ gauge theories—see also the recent work Ref. [134].

It is worth mentioning that an alternative route to the treatment of strongly coupled gauge theories has become available with the establishment of gauge-gravity dualities [135–138]. In special cases, the gravity description can capture the salient features of confinement and chiral symmetry breaking in the dual field theories [139–149]. The holographic approach to the treatment of strong dynamics has been applied to first-order phase transitions and the associated out-of-equilibrium dynamics, for example in Refs. [150–157]. We do not further discuss this approach, but refer the reader to the literature on the subject for details and insight.

Unfortunately, the emergence of first-order phase transitions presents a unique challenge to conventional lattice simulations. Metastable dynamics near criticality results in Monte Carlo (Markov chain) update methods getting stuck in one of possible multiple vacua, during the ensemble generation process. Specifically, if we call τ the Monte Carlo time needed by the system to tunnel between two vacua, while N_{conf} is the number of generated configurations, the condition $\tau \ll N_{\mathrm{conf}}$ must be fulfilled in order to obtain the correct sampling of the equilibrium distribution. This requirement leads to a dramatic increase in the number of generated configurations as the transition becomes stronger. In the approach to the infinite volume limit, in which the potential barrier separating phases grows with the system size, this critical slowing down may become an intractable numerical problem [158].

Inspired by flat histogram [158] and density of states [159] methods, the logarithmic linear relaxation (LLR) algorithm [160–163] offers a new opportunity to perform numerical studies that can be improved systematically and controllably, even in the presence of metastability, phase coexistence, tunneling, and other phenomena naturally associated with first-order phase transitions. We recall the physics principles and algorithmic processes underlying the LLR in the body of the paper. The application of the LLR algorithm to Abelian gauge theories has been studied in detail [162]. In the non-Abelian case, the properties of $SU(3)$ have been investigated at zero-temperature [163], while at finite-temperature some of the authors of this work have produced the first physical results, published in Refs. [164–166]. Finite-temperature studies exist also for $SU(4)$ [167,168] and general $SU(N)$ [169,170].

In this paper, we consider the $Sp(4)$ pure gauge theory. Following up from the minimal composite

---

[1]The calculation of the nucleation rate presents its own intrinsic challenges [74].

Higgs model proposal in Ref. [171]—see also the tables in Refs. [172–174]—and from the minimal SIMP dark-matter model proposal in Ref. [58], interest in new gauge theories with $Sp(2N)$ gauge group [in particular for $Sp(2) \sim SU(2) \sim SO(3)$ and $Sp(4) \sim SO(5)$] has motivated the development of the research program of Theoretical Explorations on the Lattice with Orthogonal and Symplectic groups (TELOS) [175–188]—see also Refs. [189–193], as well as Refs. [66–68,194–198] for dark matter models based on $Sp(4)$ gauge theories. It is hence natural to seek to characterize these theories at high temperature, starting from the Yang-Mills theory [199], to go beyond the seminal lattice work in Ref. [133].

In particular, in the following we provide the first direct lattice calculation of the nonperturbative features of the effective potential and free energy of the $Sp(4)$ theory near its confinement-deconfinement phase transition. This is input information for future calculations of out-of-equilibrium dynamical quantities, such as the nucleation rate and the relic stochastic gravitational-wave power spectrum, as anticipated. To this purpose, we develop the necessary formalism, highlight the essential features of the LLR mechanism that make this measurement possible, and perform an extensive finite volume study.

The paper is organised as follows. We define our theory in Sec. II, with particular reference to the lattice variables and action. Section III provides a self-contained, brief description of the LLR algorithm, as applied to the theory of interest. The main body of the paper starts with Sec. IV, in which we explain how to characterize the thermodynamics of the system in proximity of the phase transition and how we can extract the physical quantities of interest. Our numerical results are presented and critically discussed in Sec. V. A short outlook in Sec. VI closes the paper, except that we defer a number of important and useful technical details to the Appendix.

II. LATTICE SETUP

The continuum, Yang-Mills theory of interest has $Sp(4)$ gauge group, and lives in four space-time dimensions. The field content consists only of the gauge fields, with non-Abelian self-couplings dictated by the minimal gauge principle. To study it on the lattice, we, first, Wick rotate the Minkowski space-time and, second, discretize the resulting Euclidean space-time onto a hypercubic lattice, with spacing denoted as a, and (hyper-)volume $\tilde{V} \equiv a^4(N_t \times N_s^3)$, where $N_{t(s)}$ stands for the number of sites in the time (space) direction. We label the sites of the lattice by $(n_t, \vec{n}_s)$, where $n_t = 0, \ldots, N_t - 1$ and $\vec{n}_s = \{n_i | i = 1, 2, 3\}$, with $n_i = 0, \ldots, N_s - 1$.

The lattice link variables, $U_\mu(n_t, \vec{n}_s) \in Sp(4) \subset SU(4)$, where μ denotes the space-time direction, are matrix valued in the $Sp(4)$ group; hence they obey the relation $U_\mu \Omega (U_\mu)^T = \Omega$, with the symplectic matrix, Ω, given by

$$\Omega \equiv \begin{pmatrix} 0 & \mathbb{1}_{2\times 2} \\ -\mathbb{1}_{2\times 2} & 0 \end{pmatrix}. \tag{1}$$

This relation restricts the elements of the group to obey a block-matrix relation discussed in Appendix B.

Observables are defined as vacuum expectation values (VEVs) of operators, $O = O[U]$, that depend on the configuration of all the link variables (generically denoted as U). They are calculated as weighted averaged defined by the path integral,

$$\langle O \rangle_\beta \equiv \frac{1}{Z(\beta)} \int [DU_\mu] O[U] e^{-\beta S[U]}, \tag{2}$$

where the integral is over all possible configurations, DU_μ is the Haar measure, $S[U]$ is the classical action evaluated on a configuration, and $\beta \equiv 8/g_0^2$ is the bare coupling. The partition function is defined as

$$Z(\beta) \equiv \int [DU_\mu] e^{-\beta S[U]}. \tag{3}$$

For this study, we elect to adopt the standard (unimproved) Wilson action,

$$S[U] \equiv \frac{6\tilde{V}}{a^4}(1 - u_p[U]), \tag{4}$$

where $u_p[U]$ is the average plaquette evaluated on one lattice configuration, U.

We consider a lattice with $N_t \ll N_s$ and impose periodic boundary conditions in the temporal direction. Such a setup can be interpreted in terms of a thermalized, equilibrium system at temperature, T, determined by the inverse of the temporal extent, $T \equiv 1/(aN_t)$. For a fixed lattice size, the temperature can be altered by varying the lattice spacing, $a(\beta)$, via its dependence on the lattice coupling, β. If a phase transition takes place in the system considered at fixed temporal extension, N_t, its critical coupling, β_C, is related to the critical temperature as $T_C \equiv 1/(a(\beta_C)N_t)$. While these two quantities, T_C and β_C, can, in principle, be traded for one another, by using the aforementioned relation, in practice it is convenient to study the transition in terms of β_C, at fixed N_t. One then recovers the physical quantity, T_C, by taking the continuum limit in a way that implements also a scale-setting procedure. This can be done by building dimensionless ratios of physical observables, for example $T_c/\sqrt{\sigma}$, with σ the string tension.

The deconfinement phase transition is associated with the spontaneous breaking of the center symmetry of the group, which for all $Sp(2N)$ groups is $\mathbb{Z}_2$. The order parameter associated to this transition is the Polyakov loop, a closed loop of fundamental link variables wrapping the periodic temporal direction, normalized as follows:

$$l_p[U] \equiv \frac{1}{4N_s^3} \sum_{\vec{n}_s} \mathrm{Tr}\left(\prod_{n_t=0}^{N_t-1} U_0(n_t, \vec{n}_s)\right). \tag{5}$$

In the confined phase, this observable vanishes, while in the deconfined phase it assumes a finite value, $l_p[U] = z|l_p[U]| \neq 0$, where $z \in \mathbb{Z}_2$ is an element of the center of the group; therefore $z = \pm 1$.

In commonly used algorithms for lattice field theory calculations, vacuum expectation values are computed by replacing the path integral with an ensemble average, the configurations composing the ensemble having been generated by using importance sampling methods. In the proximity of first-order phase transitions, such algorithms are affected by metastable dynamics, so that the Monte Carlo correlation time, τ, is expected to scale exponentially with the size of the system. For a system in d dimensions, and at leading order in the linear size, L, one expects τ to scale as follows (see, e.g., the discussion in Ref. [200]):

$$\tau \propto L^\alpha e^{fL^{d-1}}. \tag{6}$$

In Eq. (6), α and f (the latter is related to the tension of the interface between the two vacua) are positive constants, dictated by the dynamics. This exponential increase of τ leads to uncontrolled systematic errors, and the resource-ineffective need to produce unmanageably large ensembles. In order to alleviate this difficulty, we utilize the LLR method, defined in the next section.

III. DENSITY OF STATES METHOD AND LLR ALGORITHM

The aim of the LLR algorithm is to estimate efficiently and accurately the density of states, $\rho(E)$, defined as

$$\rho(E) \equiv \int [DU_\mu]\delta(S[U] - E), \tag{7}$$

by sampling the space of configurations of the system, U, as a function of the energy, E. This quantity counts the number of states with a given energy (action), allowing to recast the calculation of the partition function as a one-dimensional integral over the energy,

$$Z(\beta) = \int dE \rho(E) e^{-\beta E}. \tag{8}$$

A similar reformulation applies to ensemble averages of observables that depend explicitly only on the energy,

$$\langle O \rangle_\beta = \frac{1}{Z(\beta)} \int dE \rho(E) O(E) e^{-\beta E}. \tag{9}$$

The average plaquette, u_p, is one such observable, to which we return shortly.

The numerical extraction of the density of states, $\rho(E)$, in the LLR method, starts by approximating it as a piecewise log-linear function, $\tilde{\rho}(E)$. The energy range of interest is divided into energy intervals, $E_n - \Delta_E/4 < E < E_n + \Delta_E/4$, with,

$$\log \tilde{\rho}(E) \equiv a_n(E - E_n) + c_n, \tag{10}$$

for $n = 1, \ldots, N_{\mathrm{int}}$. For sufficiently small choices of Δ_E, up to an exponentially suppressed error, the coefficients a_n and c_n must be such that $\tilde{\rho}(E) \simeq \rho(E)$. In the limit $\Delta_E \to 0$, one recovers the exact density of states, $\rho(E)$. The quantities c_n denote the value of $\log \tilde{\rho}(E)$ at the center of the intervals. By continuity of $\tilde{\rho}(E)$, they satisfy the relations,

$$c_n = c_1 + \frac{\Delta_E}{4}a_1 + \frac{\Delta_E}{2}\sum_{k=2}^{n-1} a_k + \frac{\Delta_E}{4}a_n. \tag{11}$$

Furthermore, we set $c_1 = 0$, as in most cases this factor will not affect the results. (We treat separately the observables for which this statement does not apply, such as the free energy.) In order to determine the coefficients a_n, we follow our previous work [166]. The process we employ requires the computation of the ensemble average of a known, appropriately chosen observable, and then to dial the coefficients, a_n, in order to reproduce the same result, with the replacement of $\tilde{\rho}$ in place of ρ, in Eqs. (8) and (9). The numerical algorithm is described in detail in Appendixes A and B. We repeat our determination of the coefficients on different stochastic samples and bootstrap the results to estimate uncertainties. To control the systematic error due to the finiteness of the interval, Δ_E, we repeat our calculations for multiple choices of Δ_E sizes, and extrapolate to the $\Delta_E \to 0$ limit.

The partition function is approximated, as a function of the coefficients, a_n and c_n, by the expression,

$$Z(\beta) \simeq \sum_{n=1}^{N_{\mathrm{int}}} e^{-a_n E_n + c_n} \int_{E_n - \Delta_E/4}^{E_n + \Delta_E/4} dE e^{(a_n - \beta)E}. \tag{12}$$

We can estimate expectation values of operators O as

$$\langle O \rangle_\beta \simeq \sum_{n=1}^{N_{\mathrm{int}}} \frac{e^{-a_n E_n + c_n}}{Z(\beta)} \int_{E_n - \Delta_E/4}^{E_n + \Delta_E/4} dE O(E) e^{(a_n - \beta)E}. \tag{13}$$

The probability distribution for the energy, or, equivalently, for the average plaquette, u_p, is given by

$$P_\beta(u_p) \equiv \frac{1}{Z(\beta)} \rho(E) e^{-\beta E}\bigg|_{E=\frac{6\tilde{V}}{a^4}(1-u_p)}, \tag{14}$$

and again is approximated by replacing ρ with $\tilde{\rho}$.

Once the values of a_n are known, one can sample the space of configurations with general weight, not necessarily

the Boltzmann weight appearing in the canonical ensemble. In particular, we can generate ensemble averages with flat energy distribution within narrow energy intervals—closely related to the microcanonical ensemble, but for subtleties that we discuss in the Appendix. By measuring an observable, $B[U]$, (for example, the Polyakov loop) on these configurations, we can compute the expectation values, through the equation,

$$\langle B[U]\rangle_\beta = \frac{1}{Z(\beta)}\sum_{n=1}^{N_{\text{int}}}\frac{\Delta_E}{2}\tilde\rho(E_n)\tilde B[U], \qquad (15)$$

where $\tilde B[U]$ is the vacuum expectation value for configurations restricted to the energy interval of the observable, multiplied by a weight factor,

$$\tilde B[U] \equiv \left\langle\left\langle B[U]e^{-\beta S[U]+a_n(S[U]-E_n)}\right\rangle\right\rangle_n(a_n). \quad (16)$$

IV. THERMODYNAMICS

In this section, we provide an overview of the thermodynamic observables studied in our investigation. We discuss the overall strategy we adopt to characterize the phase transition of the $Sp(4)$ pure gauge theory. General expectations suggest that the order of the phase transition should change from second to first when the number of degrees of freedom of the system exceeds a certain threshold. As the $SU(3)$ gauge theory, which has only marginally fewer degrees of freedom than $Sp(4)$, has a well-established first-order deconfinement phase transition, it is natural to expect the $Sp(4)$ Yang-Mills theory to exhibit a first-order phase transition as well, as indeed confirmed by pioneering investigations [133]. In our discussion we concentrate on the characterisation of first-order phase transitions, with the expectation (to be checked *a posteriori*) that such characterization be supported by our numerical results.

A signature of first-order phase transitions is the presence of a latent heat: a difference in internal energy between inequivalent equilibrium states coexisting at the critical temperature, T_C. It can be extracted from the discontinuity of the internal energy density, $\varepsilon(T)$, of the system, which is given by

$$\varepsilon(T) \equiv \frac{\kappa T^2}{V}\left(\frac{\partial \ln Z(T)}{\partial T}\right)_V, \qquad (17)$$

evaluated at the transition temperature, $T \to T_C$. In this expression, the partial derivative and the subsequent limit are computed at fixed volume. Hence, direct calculation of the energy density on the lattice would require the use of anisotropic lattices, to compute quantities known as Karsch coefficients [201]. Yet, if we assume the pressure to be continuous across the transition, following Ref. [124], the

latent heat can be related to the plaquette discontinuity at the critical point,

$$\frac{L_h}{T_c^4} = -\left(6N_t^4 a\frac{\partial\beta}{\partial a}\Delta\langle u_p\rangle_\beta\right)_{\beta=\beta_c}. \qquad (18)$$

We are going to follow this approach, which is consistent with the large-N arguments in Ref. [125].

In view of the potential presence of systematic effects due to how the manifestation of metastability affect the numerical study of first-order phase transitions, it is useful to consider multiple independent determinations of the same quantities, as well as the verification of known constraints among physical observables. Both strategies exploit the redundancy of the numerical measurements as a way to either cross-validate the results or provide an estimate of systematic effects. For instance, the specific heat, C_V, and the latent heat, L_h, are linked in the thermodynamic limit.

At fixed temperature and outside the critical region, we can model the plaquette fluctuations with a Gaussian probability distribution,

$$P_\beta(u_p)=A\sqrt{\frac{(\tilde V/a^4)}{C}}\exp\left(-\frac{(u_p-u_{p,0})^2\beta^2(\tilde V/a^4)}{2C}\right), \qquad (19)$$

where C is the (infinite-volume) specific heat, A is a normalization constant, and $u_{p,0}$ is the average plaquette. It is understood that C and $u_{p,0}$ are temperature-dependent. In the infinite volume limit, the distribution in Eq. (19) becomes a Dirac delta function. In the transition region, ignoring mixed phase configurations,[2] we can approximate the plaquette distribution as the sum of two Gaussians, corresponding to the two phases,

$$P_\beta(u_p) = P_\beta^{(+)}(u_p) + P_\beta^{(-)}(u_p), \qquad (20)$$

where $P_\beta^{(+)}(u_p)$ $(P_\beta^{(-)}(u_p))$ is described by parameters, $A^{(+)}$, $C^{(+)}$, $u_{p,0}^{(+)}$, $[A^{(-)}$, $C^{(-)}$, $u_{p,0}^{(-)}]$, that generalize those appearing in Eq. (19).

From the linearity of the approximation in Eq. (20), we infer that expectation values of even powers of the plaquette are the sum of their expectation values in each of the two phases,

$$\langle u_p^{2k}\rangle = \langle u_p^{2k}\rangle_+ + \langle u_p^{2k}\rangle_-, \qquad (21)$$

where $\langle\ldots\rangle_+$ denotes the expectation on the Gaussian parametrized by $A^{(+)}$, $C^{(+)}$, $u_{p,0}^{(+)}$, and $\langle\ldots\rangle_-$ is the

---

[2]These are defined by the existence of macroscopic portions of the system realizing different phases, separated by interfaces. We shall come back later to this more general case.

expectation on the Gaussian parametrized by $A^{(-)}$, $C^{(-)}$, $u_{p,0}^{(-)}$. This approximation becomes exact in the infinite volume limit, in which mixed phases are known to be absent. Therefore, for the specific heat,

$$C_V \equiv \frac{6\tilde{V}}{a^4}\left(\langle u_p^2 \rangle_\beta - \langle u_p \rangle_\beta^2\right), \qquad (22)$$

we arrive at the expectation that

$$C_V^{(\text{max})} \xrightarrow{\frac{N_t}{N_s}\to 0} \frac{6\tilde{V}}{4}\left(\Delta\langle u_p \rangle_{\beta_c}\right)^2. \qquad (23)$$

When the three-dimensional, spatial volume, V, is finite, then C_V has a maximum at a value of the coupling, that we denote as $\beta_{CV}(C_V)$. The value of the maximum diverges, in the approach to the thermodynamic limit, proportionally to the volume. This provides an operational way to determine the critical coupling, β_C, at fixed N_t,

$$\beta_C(N_t) = \lim_{N_s\to\infty} \beta_{CV}(C_V). \qquad (24)$$

Any susceptibility (or susceptibilitylike observable coupling to the degrees of freedom that are relevant for the transition) is expected to be characterised by a finite-volume peak or dip, the value of which diverges in the thermodynamic limit. The position of the peak provides a finite-volume definition of a pseudocritical coupling, that converges to the critical value in the infinite-volume limit. An additional energy-based observable characterizing phase transitions is the Binder cumulant [202,203], defined as

$$B_V(\beta) \equiv 1 - \frac{\langle u_p^4 \rangle_\beta}{3\langle u_p^2 \rangle_\beta^2}. \qquad (25)$$

For first-order phase transitions, in the thermodynamic limit, a minimum appears at the critical coupling, $\beta_{CV}(B_V)$.[3]

Similar arguments hold for the susceptibility of the Polyakov loop,

$$\chi_l(\beta) \equiv N_s^3\left(\langle |l_p^2| \rangle_\beta - \langle |l_p| \rangle_\beta^2\right), \qquad (26)$$

which has a finite-volume maximum at the pseudocritical value of the coupling, $\beta_{CV}(\chi_l)$. While at fixed V the three pseudocritical couplings we introduced, $\beta_{CV}(C_V)$, $\beta_{CV}(B_V)$, and $\beta_{CV}(\chi_l)$, are in general different, they must all converge to the same β_C in the thermodynamic limit, at fixed N_t.

---

[3]In the case of first order phase transitions, the value of the minimum in B_V converges to a finite value in the infinite volume limit. By contrast, for continuous phase transitions B_V approaches a value of $2/3$, and the dip around the critical coupling disappears.

Another important observable characterising first-order phase transitions is the tension of the interface separating coexisting equilibrium phases. It can be extracted from the measurement of the plaquette distribution. Specifically, at finite volume, if we consider the value of β for which the two peaks of the distribution have the same height, P_{max}, the confinement-deconfinement interface tension, σ_{cd}, can be extracted from the relation,

$$\frac{P_{\text{min}}}{P_{\text{max}}} \propto N_s^{\frac{1}{2}} \exp\left(-2\frac{\sigma_{cd}}{T_C^3}\frac{N_s^2}{N_t^2}\right), \qquad (27)$$

where P_{min} is the value of the probability at the minimum located between the maxima. For a heuristic derivation of this expression, see, e.g., Ref. [124].

It is important to highlight that the contribution to the probability distribution of these interfaces is not captured by the double Gaussian approximation, Eq. (20), as the former is due to a macroscopic, emergent interaction between subsystems, while the latter approximates the mixed-phase system in terms of two independent, free subsystems. Nevertheless, the argument leading to Eq. (23) remains asymptotically correct. Note also that, in the derivation of Eq. (27) in Ref. [124], effects such as the vibration of the interface are not considered; yet, these and other effects we ignore, including the unknown proportionality factor, are expected to be suppressed as N_s^{-2}. Therefore, we can extract the interface tension from the quantity,

$$\tilde{I} \equiv -\frac{N_t^2}{2N_s^2}\log\left(\frac{P_{\text{min}}}{P_{\text{max}}}\right) - \frac{N_t^2}{4N_s^2}\log(N_s), \qquad (28)$$

by taking the limit $N_t/N_s \to 0$,

$$\lim_{\frac{N_t}{N_s}\to 0} \tilde{I} = \tilde{\sigma}_{cd}, \qquad (29)$$

where, for convenience, we have defined $\tilde{\sigma}_{cd} = \sigma_{cd}/T_C^3$.

The process of determining $\tilde{I}$ through the plaquette probability distribution in the critical region introduces a fourth definition of the finite-volume pseudocritical β as the value at which the peaks of the plaquette distribution are equal. We call this value β_{CV}.

The LLR approach gives us access to thermodynamic observables that are exponentially (in the volume) hard to determine using importance sampling methods. Using analogies with statistical physics, we define the free energy, F, entropy, s, and temperature, t, of the microstates as

$$F \equiv E - ts, \quad s = \log(\rho), \quad t = \frac{\partial E}{\partial s} = \frac{1}{a_n}, \qquad (30)$$

where the internal energy, E, is given by the total action. As in classical thermodynamics, both s and E are state

functions, defined up to an additive constant. In Eq. (11), we have arbitrarily set the value of c_1; therefore the calculated value of the free energy will differ from the true value by a term linear in temperature. As we are mostly interested in calculating the difference in the free energy at fixed temperatures, we can arbitrarily choose this value. We define a reduced free energy, $f(t)$, to remove this first arbitrariness,

$$f(t) \equiv \frac{a^4}{\tilde{V}} (F(t) + \Sigma t), \qquad (31)$$

with Σ the average entropy of the microstates.

As we shall see in our numerical results, with this definition the swallow-tail structure of $f(t)$, characteristic of first-order transitions, becomes prominent. This structure is the result of physically different microstates coexisting at the same temperature, over a finite range of t, close to criticality. In addition to the unstable branch, the coexistence phenomenon gives rise to two metastable branches, corresponding, respectively, to the confined and deconfined states at temperatures where they have a higher free energy than the true equilibrium state. We call f_c^+ the value of the reduced free energy evaluated at the point at which the two metastable branches cross. The value of β at which this happens (at finite volume) gives rise to a fifth definition of the pseudocritical temperature, which we call $\beta_{CV}(f)$. For further discussion of the structure of the free energy and our approach to determining it, see also our previous work, in Ref. [166]. By comparing the definition of Eq. (14) with the free energy, we arrive at the relation,

$$\exp\left(-\frac{F(t)}{t}\right) = Z(\beta)P_\beta(E)\bigg|_{\beta=1/t, E=F(t)+ts}, \qquad (32)$$

where $P_\beta(E)$ corresponds to the probability of being in a given microstate with internal energy E, for $t = 1/\beta$. Therefore, this definition of the critical coupling $\beta_{CV}(f)$, should be equivalent to β_{CV} even at finite volume.

V. RESULTS

This section contains the main body of the paper. We restrict attention to the characterization of the finite-temperature, deconfinement phase transition of the $Sp(4)$ Yang-Mills lattice theory. We consider a fixed extent of the temporal direction, $N_t = 4$, and study the extrapolation of our results towards the thermodynamic limit, by varying the number of sites in the spatial directions, $N_s = 20, 24, 28, 40, 48$.

As a preliminary step, before carrying out a full, high precision, LLR analysis, we use standard importance sampling methods to determine the region of interest in the lattice coupling, β. By doing so, we set the plaquette range $(u_p)_{\min} < u_p < (u_p)_{\max}$ that will be explored by the LLR algorithm and at the same time set initial values for the

coefficients, $\{a_n^{(0)}\}_{n=1}^{N_{\text{int}}}$, that will then be determined to high precision by our numerical, iterative processes. We carry out a standard importance sampling parameter scan of β values around the critical coupling, for a lattice with extent $N_t \times N_s^3 = 4 \times 20^3$. In Ref. [133], the critical inverse coupling for $N_t = 4$, in the thermodynamic limit, was determined to be $\beta_C = 7.339(1)$. Therefore, we choose in this scan the values $\beta = 7.32, 7.33, 7.335, 7.34, 7.345, 7.35$.

By measuring the ensemble average of the absolute value of the Polyakov loop, as well as the average plaquette, we determine that the range of values of β of interest is $7.33 < \beta < 7.35$. With this information at hand, by inspecting the histogram of measured average plaquette values, we determine the required plaquette range of interest to be $(u_p)_{\min} = 0.565 < u_p < (u_p)_{\max} = 0.585$. As the volume increases, we expect the plaquette distribution to become more constrained, and therefore for larger volumes we restrict this range to $(u_p)_{\min} = 0.568 < u_p < (u_p)_{\max} = 0.576$.

We list in Table I the parameters used in each of our LLR calculations for the $Sp(4)$ lattice theory, with $N_t = 4$. On the smaller lattices, we choose two different configurations for the LLR algorithm, by changing the number of subintervals intervals, N_{int}, and the total range of plaquette, u_p, considered. We do so to be able to demonstrate that the calculations are performed in the asymptotic regime of the $\Delta_{u_p} \to 0$ extrapolation. More details and discussions are given in Appendix D. As in Ref. [166], we extrapolate the results linearly in $\Delta_{u_p}^2$, to approach the $\Delta_{u_p} \to 0$ limit. For $N_s = 48$, due to computational resources we have results for a single interval size. For $N_t = 5$, we list some of the available information in Appendix C—see Table II—but a large scale, high precision analysis is postponed to future publications.

An estimate for $a_n(u_p)$, used as initial condition for the LLR algorithm, is obtained as follows. We focus at first only on lattices with $\tilde{V}/a^4 = 4 \times 20^3$. We use standard importance sampling methods to compute $\langle u_p \rangle_\beta$, for the six values of β listed earlier on. We then fit the result with a cubic polynomial, and invert the outcome (locally) to obtain a function, $\beta(u_p)$. For each lattice volume, and each choice of plaquette intervals, we then identify the middle point, $(u_p)_n$, of the $n = 1, \ldots, N_{\text{int}}$ subintervals. The corresponding values of the fitted $\beta((u_p)_n)$ are finally used as to compute a first (rough) estimate of the coefficients, $\{a_n^{(0)}\}_{n=1}^{N_{\text{int}}}$.

As described in Appendix A—to which we refer for more details—the LLR algorithm takes the aforementioned initial value of $\{a_n^{(0)}\}_{n=1}^{N_{\text{int}}}$, and improves them iteratively, by applying at first the Newton-Raphson (NR) method, followed by the Robbins-Monro (RM) method. By monitoring the NR trajectories of the coefficients, we find that

TABLE I. List of $Sp(4)$ lattice ensembles with extension in the time direction $N_t = 4$. For each of them, we list the lattice extension, $N_t \times N_s^3$, the number of (overlapping) subintervals, N_{int}, the number of replicas, n_R, the extent of the interval in average plaquette, Δ_{u_p}, and the maximum and minimum values of the plaquette, $(u_p)_{\min}$ and $(u_p)_{\max}$. We also report the number of iterations defined in Appendix A: $\bar{m}$, $\tilde{m}$, $\hat{m}$, n_{Th}, n_M, and n_{fxa}.

$N_t \times N_s^3$	N_{int}	n_R	Δ_{u_p}	$(u_p)_{\min}$	$(u_p)_{\max}$	$\bar{m}$	$\tilde{m}$	$\hat{m}$	n_{Th}	n_M	n_{fxa}
4×20^3	48	20	0.00064	0.565	0.58	10	300	100	300	700	100
4×20^3	64	20	0.00048	0.565	0.58	10	300	100	300	700	100
4×24^3	48	20	0.00064	0.565	0.58	10	300	100	300	700	100
4×24^3	64	20	0.00048	0.565	0.58	10	300	100	300	700	100
4×28^3	64	20	0.00048	0.565	0.58	10	200	100	300	700	100
4×28^3	64	20	0.00025	0.568	0.576	10	200	100	300	700	100
4×40^3	96	25	0.00017	0.568	0.576	10	100	50	300	700	100
4×40^3	128	25	0.00013	0.568	0.576	10	100	50	300	700	100
4×48^3	128	25	0.00013	0.568	0.576	10	100	50	300	700	100

TABLE II. List of $Sp(4)$ lattice ensembles with extension in the time direction $N_t = 5$. For each of them, we list the lattice extension, $N_t \times N_s^3$, the number of (overlapping) subintervals, N_{int}, the number of replicas, n_R, the extent of the interval in average plaquette, Δ_{u_p}, and the maximum and minimum values of the plaquette, $(u_p)_{\min}$ and $(u_p)_{\max}$. We also report the number of iterations defined in Appendix A: $\bar{m}$, $\tilde{m}$, $\hat{m}$, n_{Th}, n_M, and n_{fxa}.

$N_t \times N_s^3$	N_{int}	n_R	Δ_{u_p}	$(u_p)_{\min}$	$(u_p)_{\max}$	$\bar{m}$	$\tilde{m}$	$\hat{m}$	n_{Th}	n_M	n_{fxa}
5×48^3	48	25	0.00017	0.5875	0.5915	10	60	50	300	700	100
5×48^3	96	25	0.00008	0.5875	0.5915	10	50	50	300	700	100
5×56^3	48	25	0.00017	0.5875	0.5915	10	50	50	300	700	100
5×56^3	96	25	0.00008	0.5875	0.5915	10	50	50	300	700	100
5×56^3	128	25	0.00006	0.5875	0.5915	10	50	50	300	700	100

$\bar{m} = 10$ iterations of the NR method evolve the coefficients sufficiently close to the true value as to be able to swap to the RM method. We choose the total number of RM iterations by balancing considerations such as computing time constraints and accuracy goals of this study. For the smallest lattices, we carry out $\tilde{m} = 300$ RM iterations, reduced to $\tilde{m} = 100$ for the largest lattice volumes available. In all cases, we verify that the result is converging to the same value at approximately the asymptotic scaling for RM iterations, $1/\sqrt{m}$.

In Fig. 1, we display the final values of the coefficients, a_n, obtained with the numerical algorithm, as a function of the plaquette value measured at the center of each subinterval, $(u_p)_n$. The figure shows the results obtained with the smallest choice of subinterval size, Δ_{u_p}, for each of the available spatial volumes. The plot shows only a detail of the critical region, signalled by the noninvertibility of $a_n(u_p)$. This is a global manifestation of the metastable dynamics characteristic of a first order transition. As the lattice volume increases, the region of u_p for which $a_n(u_p)$ is not invertible increases in extent, and its manifestation sharpens. The coefficients a_n must be volume independent [162]; hence these are systematic, finite-volume effects that degrades the quality of the measurements, and must be

minimized. For particularly small volumes, one might even miss the noninvertibility signal, which would become fainter and more difficult to measure. By contrast, as the figure shows, with our choices of parameters, subintervals, and analysis strategy, the results converge well towards the thermodynamic limit, $N_s \rightarrow +\infty$.

By using the coefficients a_n, we compute the thermodynamic potentials Eq. (30). By piecewise inverting $a_n(u_p)$, and using Eq. (31), to find $E(t)$, $s(t)$ and therefore the (reduced) free-energy, $f(t)$, which we then show in Fig. 2, for the same choices of volume and subintervals as in Fig. 1. In doing so, we set the additive integration constant, Σ, appearing in the entropy, s, to be equal to the average entropy across all intervals.[4] The points on the plot show the values for the center of each interval, with errors in both the value of the reduced free energy and the (microcanonical) temperature, calculated by bootstrapping over n_R repeats of the LLR algorithm. The lines are found by piecewise linearly interpolating in the interval between the available points for $a_n((u_p)_n)$.

---

[4]This choice leads to the visible difference in rotation of the tail of the diagram for $N_s = 20$ and $N_s = 24$, which is due to the difference in the range of plaquette used in the calculation of Σ.
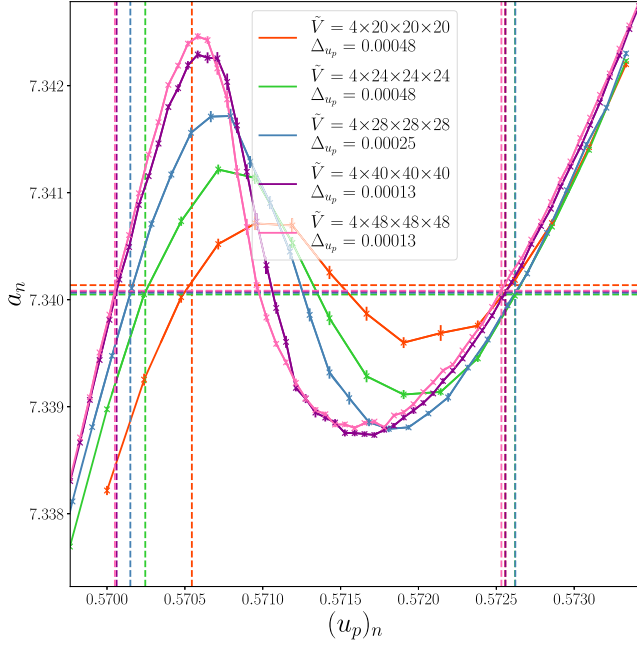
FIG. 1. Measured coefficients, a_n, as a function of the plaquette value at the center of the energy subinterval, $(u_p)_n$, for the $Sp(4)$ theory, for lattices with temporal size of $N_t = 4$, and spatial sizes $N_s = 20, 24, 28, 40, 48$ (color coded). The size of the subinterval sizes, for each of the spatial volumes, is given by $\Delta_{u_p} = 0.00048$, 0.00048, 0.00025, 0.00013, 0.00013, respectively. The plot displays a portion of the available data, highlighting the critical region, in which the noninvertibility of $a_n((u_p)_n)$ is manifest. The horizontal dashed lines shows the critical coupling, $a_n = \beta_{CV}(f)$, estimated in the study of the reduced free energy density, f. The vertical lines show the corresponding plaquette values.

FIG. 2. The reduced free energy density, f, plotted as a function of the microcanonical temperature, $t = 1/a_n$, for lattices with temporal size $N_t = 4$, spatial sizes $N_s = 20, 24, 28, 40, 48$ (color coded). The subintervals have sizes $\Delta_{u_p} = 0.00048$, 0.00048, 0.00025, 0.00013, 0.00013, respectively. To ensure that the (reduced) free energy difference is directly comparable between lattice sizes, a constant term, f_c^+, has been subtracted from f. This is defined so that all reduced free energies vanish at the transition, the point in which the two metastable branches cross. The vertical lines show the crossing points between metastable branches, which identifies the critical temperature. The horizontal lines denote the value of the free energy density along the unstable branch, evaluated at criticality.

This is possibly the most important, certainly the most beautiful result of this study, displayed in Fig. 2. The free energy density, f, displays the swallow-tail structure that is characteristic of a first-order transition. Away from the critical region, f is single valued, corresponding to plaquette values, or energies, for which only one single phase exists. In the critical region, there are two coexisting metastable branches, each corresponding to pure phase states, and an unstable, mixed phase branch, having the largest free energy. We observe that the region exhibiting metastable dynamics grows with the volume as does the difference in free energy between the unstable and metastable branches. Yet, it appears to converge in the thermodynamic limit, $N_s \to +\infty$.

From Fig. 2, the reciprocal of the (microcanonical) temperature, t, at which the two metastable branches cross, or equivalently the value of the coefficient, a_n, for which this happens, provides a measurement of the critical coupling of the system, $\beta_{CV}(f) = 1/t_c$. At this value, the plaquette distribution has a double Gaussian structure with two peaks of equal height. Numerically, we determine the critical point by finding the value of t which minimizes the difference in free-energy between the two metastable
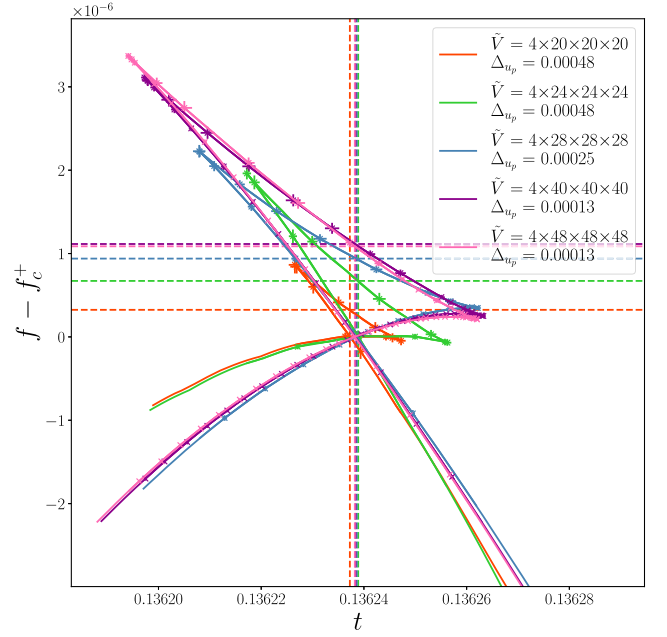
branches. Uncertainties, as elsewhere, are computed by bootstrapping over the results for the n_R repeats. Having determined the critical coupling, we compute the reduced free energy of the metastable branch at the critical point, f_c^+. As we are only interested in the free-energy difference between the microstates at the same temperature, and we want to compare different calculations across volumes, we remove a second additive integration constant, in f, by subtracting the f_c^+. The horizontal lines in Fig. 2 show the value of the reduced free-energy on the unstable branch at the critical point.

From the properties of the reduced free energy density we can also compute the other two main thermodynamic observables characterising the transition. For the interface tension, the logarithmic term in Eq. (28), which determines $\tilde\sigma_{cd}$ via Eq. (29), is related to the difference, Δf, in the (reduced) free energy between the unstable and metastable branches at the critical point, $\log(P_{\max}/P_{\min}) = (\tilde V/a^4)\Delta f/t_c$. For the latent heat, we need to measure the discontinuity in the plaquette at the critical point, $\Delta\langle u_p\rangle_{\beta_{CV}}$. It can be extracted from the function $u_p(a_n)$,
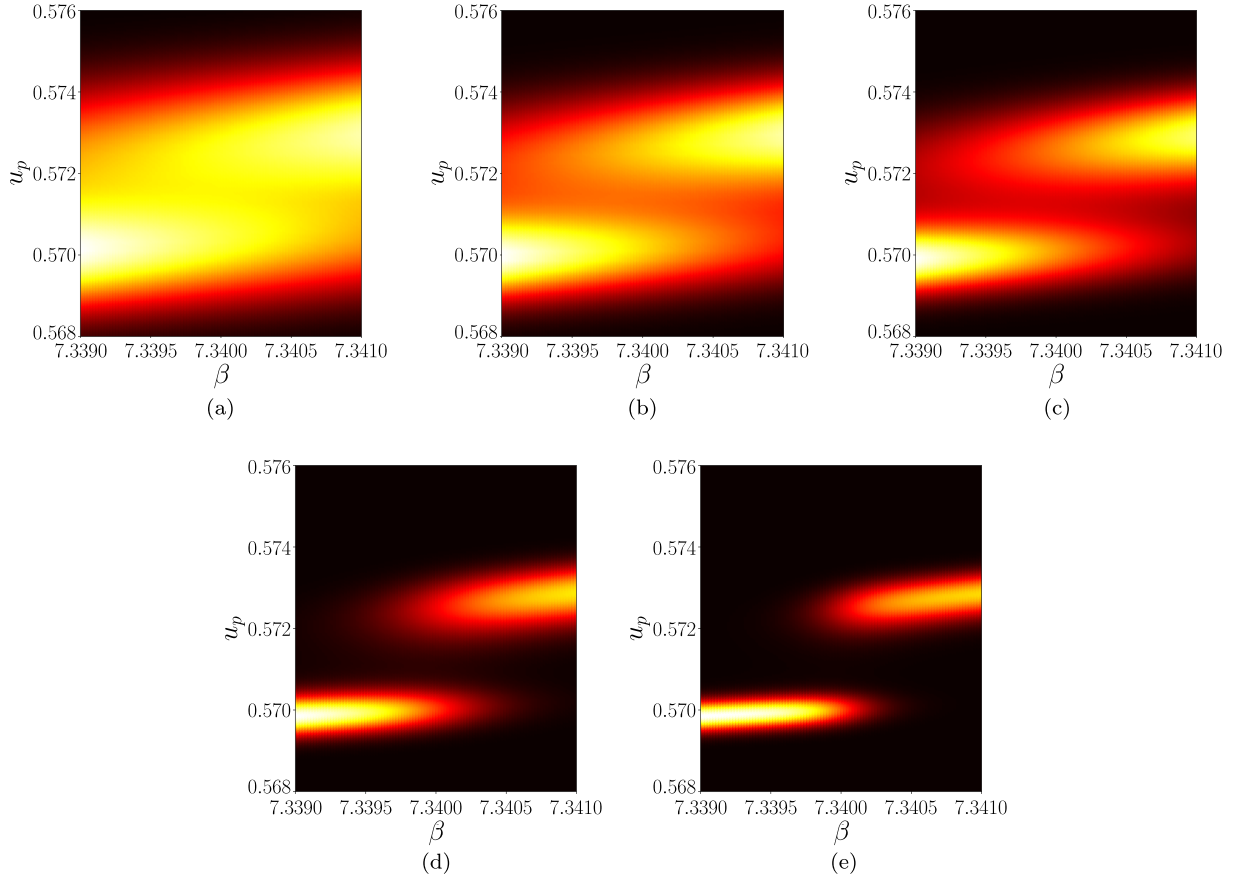
FIG. 3.   The plaquette probability distribution, $P_\beta(u_p)$, displayed as a color map in the plane of coupling, β, and plaquette value, u_p. Darker colors represent lower $P_\beta(u_p)$ values. The temporal lattice size is $N_t = 4$, with different spatial sizes, $N_s = 20, 24, 28, 40, 48$, and with subinterval sizes $\Delta_{u_p} = 0.00048, 0.00048, 0.00025, 0.00013, 0.00013$, respectively. The plaquette range displayed in all plots is $0.568 < u_p < 0.576$, with coupling in the range $7.339 < \beta < 7.341$. The lattice volumes shown are: (a) $\tilde{V}/a^4 = 4 \times 20^3$, $\Delta_{u_p} = 0.00048$. (b) $\tilde{V}/a^4 = 4 \times 24^3$, $\Delta_{u_p} = 0.00048$. (c) $\tilde{V}/a^4 = 4 \times 28^3$, $\Delta_{u_p} = 0.00025$. (d) $\tilde{V}/a^4 = 4 \times 40^3$, $\Delta_{u_p} = 0.00013$. (e) $\tilde{V}/a^4 = 4 \times 48^3$, $\Delta_{u_p} = 0.00013$.

presented in Fig. 1. In this plot the horizontal dashed line shows $a_n = \beta_{CV}(f)$, the vertical lines show the plaquette values which intercept this line, $u_p(a_n = \beta_{CV}(f))$, along the metastable branches. These two values correspond to the peaks of the plaquette distribution at the critical point. Their difference is the jump (discontinuity) in the plaquette.

We can compute the distribution probability of the plaquette, $P_\beta(u_p)$, for any value of the coupling in the range for which we computed the coefficients a_n, by using Eq. (14), with ρ replaced by $\tilde{\rho}$, the latter being determined by the measured values of a_n. The color maps in Fig. 3 show the resulting plaquette distribution, as reconstructed from the LLR algorithm, in the critical region between $7.339 < \beta < 7.341$. Starting from the lowest value of the coupling, β, each plot displays the presence of a single peak, corresponding to a single available phase for the system. The peak decreases in size and spreads out when increasing β. A second peak starts to appear and grows until it has equal height to the first peak, at the critical coupling (towards the middle of the plots). Then, as the coupling is

increased further, the new peak from the high temperature phase starts to dominates the system while the original peak starts to fade. Ultimately, at the right-hand of the range of β displayed, only the distribution due to the new phase is still visible. As the spatial volume grows, the width of the peaks decreases and the height of the peak grows. It is expected they will become Dirac delta distributions in the thermodynamic limit.

Looking only at Fig. 3, one might incorrectly infer that the probability distribution vanishes in the area between the peaks. However, in Fig. 4 one can see that there remains a finite probability between the peaks, at criticality, for all spatial volumes. As the volume increases, the peak of the distribution grow while their width decreases. While for the smallest volumes the whole distribution can be approximated as a double Gaussian, this approximation fails at larger volumes, as the region between the peaks displays a finite plateau.

Figure 5 demonstrates this phenomenon, for the largest volume available, and for subintervals with width
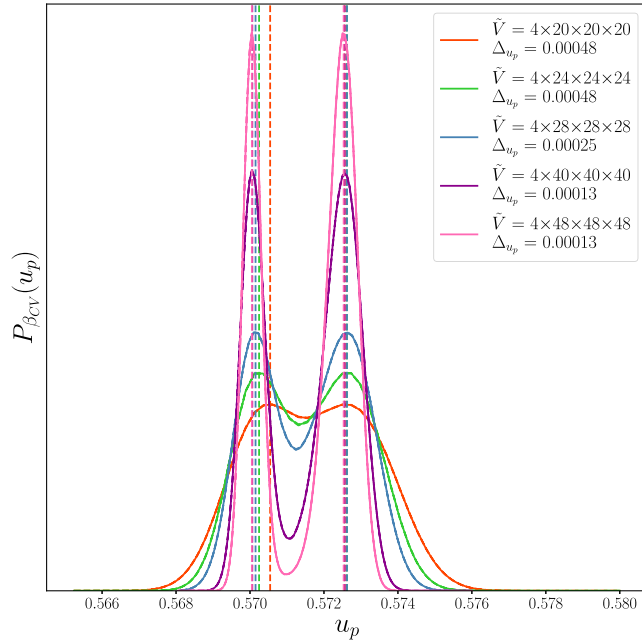
FIG. 4. The plaquette probability distribution, $P_\beta(u_p)$, computed at the critical point, $\beta = \beta_{CV}(f)$, exhibiting a double peak structure with peaks of equal height. The plot shows results for lattice systems with temporal extent $N_t = 4$, spatial sizes, $N_s = 20, 24, 28, 40, 48$, (color coded), and subinterval sizes $\Delta_{u_p} = 0.00048, 0.00048, 0.00025, 0.00013, 0.00013$, respectively. The vertical dashed lines show the location of the peaks of the distribution.
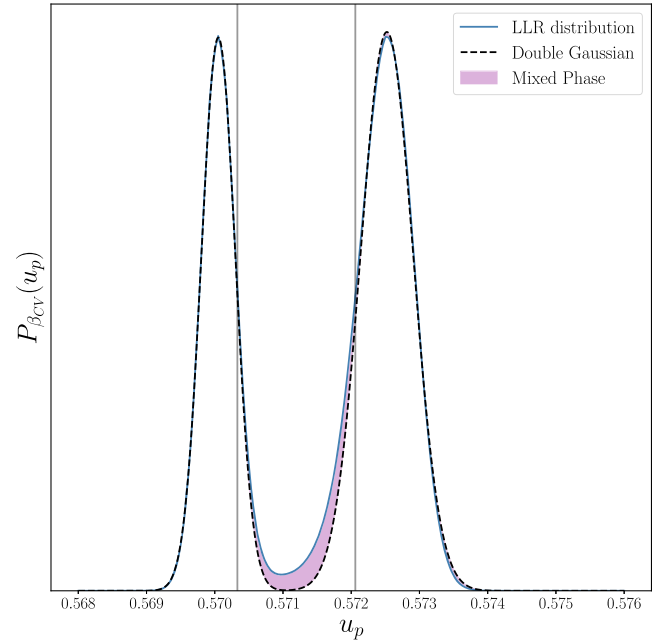

FIG. 5. The plaquette probability distribution, $P_\beta(u_p)$, computed at the critical point, $\beta = \beta_{CV}(f)$, and exhibiting a double peak structure with peaks of equal height. The plot shows results for a lattice systems of volume $\tilde{V}/a^4 = 4 \times 48^3$, with interval sizes $\Delta_{u_p} = 0.00013$. The black dashed line shows a fitted double Gaussian function to the observed plaquette distribution reconstructed from the LLR results, in blue. The double Gaussian is fitted to the region outside the gray vertical lines, therefore excluding the central dip. The difference between the observed plaquette distribution and the fitted double Gaussian is highlighted in pink.

$\Delta_{u_p} = 0.00013$. We fit a double Gaussian to the LLR results, but exclude from the fit the central region, between vertical lines. The double Gaussian approximation holds well in the external region, included in the fit. However, in the internal region the double Gaussian vanishes, while the LLR distribution converges to a constant. We expect the primary reason for this difference to be due to the presence of mixed phase states and the interface tension between them.

To quantify the effect of the interface terms, we compute the quantity $\tilde{I}$, defined in Eq. (28), which relates to the interface tension, $\tilde{\sigma}_{cd}$, and therefore the probability of tunneling between phases. We compute the logarithmic term, $\log(P_{\text{max}}/P_{\text{min}})$, in terms of the change in free-energy, as explained earlier. Errors are, again, computed by bootstrapping the results over the values found for the n_R independent repeats. To remove finite interval systematic effects, we extrapolate the results to the limit of vanishing interval size, for each spatial volume. Details are provided in Appendix D. The measured values of $\tilde{I}$ are presented in Fig. 6, as a function of the square of the inverse of the aspect ratio, $(N_t/N_s)^2$. We fit a quadratic polynomial in $(N_t/N_s)^2$ to our numerical results, excluding the smallest volume, $N_s = 20$, and extrapolate to the thermodynamic limit, $(N_t/N_s) \to 0$. The reduced chi-square for

the fit is given by $\chi^2/N_{\text{d.o.f.}} = 1.0$, and the extrapolation gives $\tilde{\sigma}_{cd} = \lim_{N_t/N_s \to 0} \tilde{I} = 0.01718(32)(1).$[5] As a side remark, we note that in the case of the two largest available volumes, with $N_s = 40$ and $N_s = 48$, the term logarithmic in N_s dominates in Eq. (28), and their subtraction is essential. Therefore, it is possible that only the final two points are close enough to the asymptotic regime (the thermodynamic limit). Yet, the overall trend of the data does not display reasons for concern, with current uncertainties.

We can reconstruct canonical observables using Eq. (9), for observables with explicit dependence on the energy, and Eq. (15), for more general observables. We display some interesting results of this type of analysis in Figs. 7–10, and comment about them in the following.

We compute the average plaquette, $\langle u_p \rangle_\beta$, and the absolute value of the Polyakov loop, $\langle |l_p| \rangle_\beta$, for a selection of couplings, β, around the critical point, and display the

---

[5]The second bracket denotes an additional systematic uncertainty coming from the chosen parametrization of the thermodynamic limit, as discussed in Appendix E.
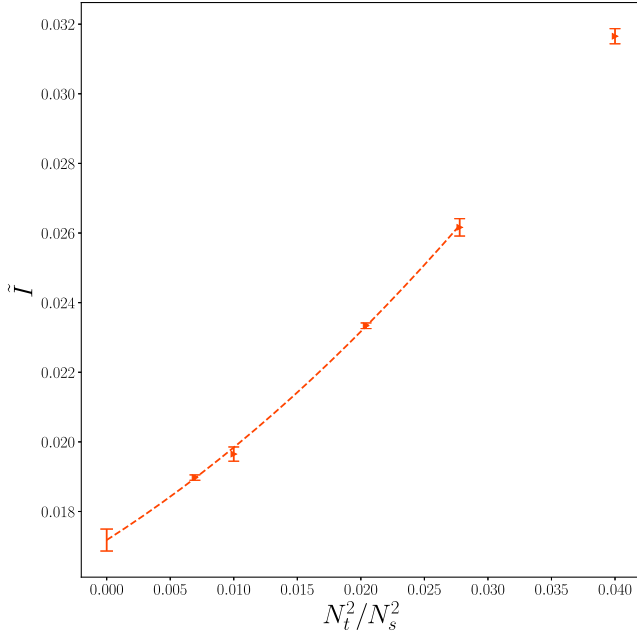
FIG. 6. The interface term, $\tilde{I}$, defined in Eq. (28), plotted against the square of the inverse of the aspect ratio, N_t^2/N_s^2, for lattices with temporal extent $N_t = 4$, and spatial sizes $N_s = 20$, 24, 28, 40, 48. For each spatial volume, we show the result of the extrapolation to the limit of vanishing subinterval size—see Appendix D. The dashed line shows a polynomial fit in N_t^2/N_s^2 of the points with the four largest spatial volumes. The reduced chi square is $\chi^2/N_{\text{d.o.f.}} = 1.0$. We also display the extrapolated $\lim_{N_t/N_s \to 0} \tilde{I} = 0.01718(32)(1)$.

FIG. 7. The VEV of the average plaquette, $\langle u_p \rangle_\beta$, plotted as a function of coupling, β, for lattices with temporal size, $N_t = 4$, spatial sizes $N_s = 20$, 24, 28, 40, 48 (color coded), and subinterval sizes $\Delta_{u_p} = 0.00048$, 0.00048, 0.00025, 0.00013, 0.00013, respectively. We chose a grid with 1000 evenly spaced values of β, in the interval $7.337 < \beta < 7.343$, for $N_s = 20$, 24, and 28, and $7.339 < \beta < 7.341$, for $N_s = 40$ and 48.

results in Figs. 7 and 8. As the spatial volume increases, the results for these observables approximate the discrete jump one expects in a first-order phase transition. This transition is quantified by the specific heat, $C_V(\beta)$, for the average plaquette, and the Polyakov loop susceptibility, $\chi_l(\beta)$. We display our results for these quantities in Figs. 9 and 10, respectively. In proximity of a first-order phase transition, we expect the peak of the specific heat, $C_V^{(\text{max})}$, and Polyakov loop susceptibility, $\chi_l^{(\text{max})}$ to scale with the spatial volume of the system. In both cases, the peak grows and the width decreases with the volume. We measure the values at the peak, $C_V^{(\text{max})}$, and $\chi_l^{(\text{max})}$, as well as the critical couplings, $\beta_{CV}(C_V)$ and $\beta_{CV}(\chi_l)$, by taking the maximum observed value in our scan of β values. We estimate the errors by bootstrapping the results for the n_R repeats.

Another important quantity in the study of first order phase transitions is the Binder cumulant, $B_V(\beta)$, defined in Eq. (25). At the critical point, this quantity exhibits a minimum, $B_V^{(\text{min})}$, in correspondence of the critical coupling, $\beta_{CV}(B_V)$, which we compute by taking the minimum observed value from a scan of β values. Figure 11 shows this quantity, measured in a neighborhood of the phase transition, for several choices of spatial volume. Although
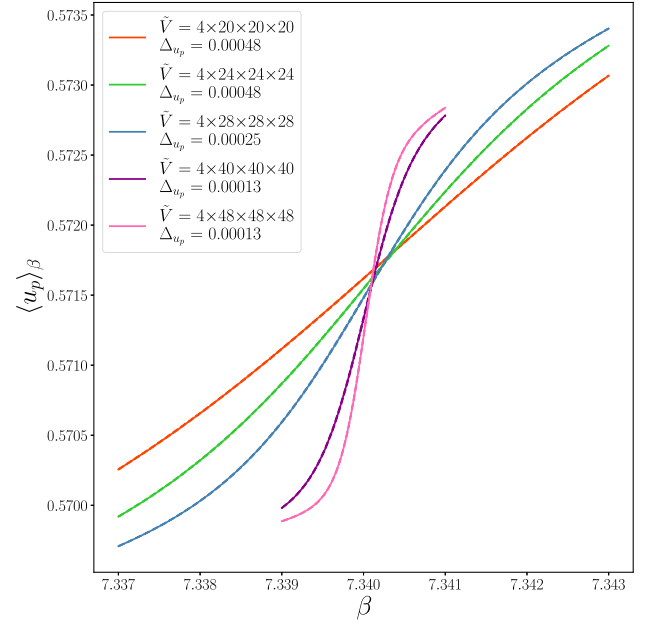
the dip reduces as the volume grows, it stays finite, and appears to converge.

We have analyzed our data by exploiting four alternative definitions for the critical point of the phase transition: the coupling for which the free energy of the two metastable branches are equal, $\beta_{CV}(f)$, the coupling corresponding to the peak of the specific heat, $\beta_{CV}(C_V)$, to the maximum of the Polyakov loop susceptibility, $\beta_{CV}(\chi_l)$, and to the minimum of the Binder cumulant, $\beta_{CV}(B_V)$. Due to the presence of finite volume effects, we expect discrepancies of order $\mathcal{O}(1/N_s^3)$ to appear at finite volume, but we also expect all definitions to converge to one result in the thermodynamic limit. Nevertheless, while correlations must be present (as we measure the density of states just once, on a common set of numerical data), we can use the resulting four different estimates to assess the size of systematic effects appearing due to the methodology adopted in the measurement of the critical coupling. As we shall see, we find these systematic effects to have comparable size to the statistical errors, and hence they cannot be neglected.

Figure 12 shows the measurements of these four critical couplings, for each available spatial volume, as a function of the cube of the inverse of the aspect ratio, N_t^3/N_s^3. In each case, we have first extrapolated towards the limit of vanishing interval size—see Appendix D. For each definition, we fit the measurements to a linear function
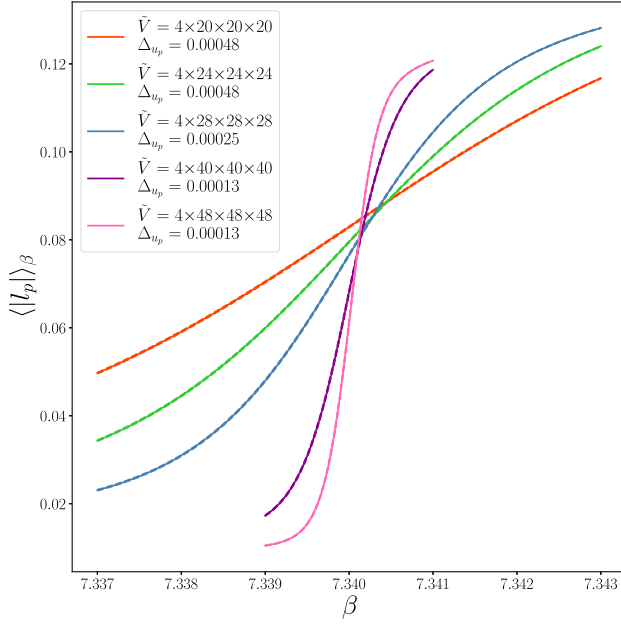
FIG. 8. The VEV of the absolute value of the Polyakov loop, $\langle |l_p| \rangle_\beta$, plotted as a function of coupling, β, for lattices with temporal size, $N_t = 4$, spatial sizes $N_s = 20, 24, 28, 40, 48$ (color coded), and subinterval sizes $\Delta_{u_p} = 0.00048, 0.00048, 0.00025, 0.00013, 0.00013$, respectively. We chose a grid with 100 evenly spaced values of β, in the interval $7.337 < \beta < 7.343$, for $N_s = 20, 24,$ and 28, and $7.339 < \beta < 7.341$, for $N_s = 40$ and 48.

FIG. 9. The specific heat, $C_V(\beta)$, plotted as a function of coupling, β, for lattices with temporal size, $N_t = 4$, spatial sizes $N_s = 20, 24, 28, 40, 48$ (color coded), and subinterval sizes $\Delta_{u_p} = 0.00048, 0.00048, 0.00025, 0.00013, 0.00013$, respectively. We chose a grid with 1000 evenly spaced values of β, in the interval $7.337 < \beta < 7.343$, for $N_s = 20, 24,$ and 28, and $7.339 < \beta < 7.341$ for $N_s = 40$ and 48.

(excluding the measurement with $N_s = 20$). We extrapolate all fits to the limit $N_t/N_s \to 0$. The extrapolation for the peak of the specific heat and minima of the Binder cumulant yield $\beta_C(C_V) = 7.340018(7)(5)$ and $\beta_C(B_V) = 7.340019(7)(5)$, with reduced chi-squared of $\chi^2/N_{\text{d.o.f.}} = 0.84$ and $\chi^2/N_{\text{d.o.f.}} = 0.81$ respectively. The resulting agreement is not surprising, as both definitions are based on the behavior of the average plaquette; even at finite volume the measurements are consistent with each other.

The extrapolation of the critical coupling taken from the peak of the Polyakov loop susceptibility yields $\beta_C(\chi_l) = 7.340052(8)(4)$, with reduced chi-square of $\chi^2/N_{\text{d.o.f.}} = 0.26$. This lies outside the error of the specific heat and Binder cumulant extrapolation; however the final point, at finite volume, is within error of the others. This discrepancy could be due the extrapolations not considering the higher-order effects on the finite-size scaling, due to the presence of mixed phase states.

The final extrapolation to the thermodynamic limit is given by $\beta_C(f) = 7.340089(8)(2)$, which has a reduced chi-square of $\chi^2/N_{\text{d.o.f.}} = 0.08$. The reduced chi-square is very small in this fit and might be due to an overestimation of the errors. The result for this definition of the critical coupling is not consistent with the other ones, at either finite volume nor after extrapolations.
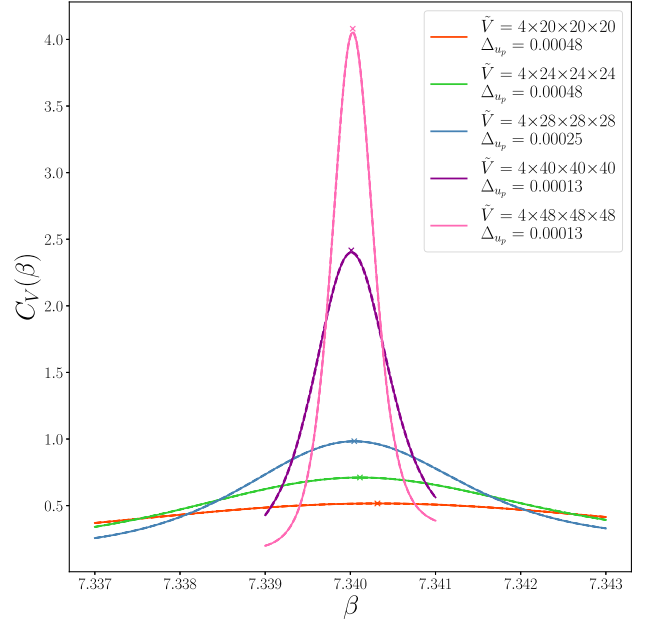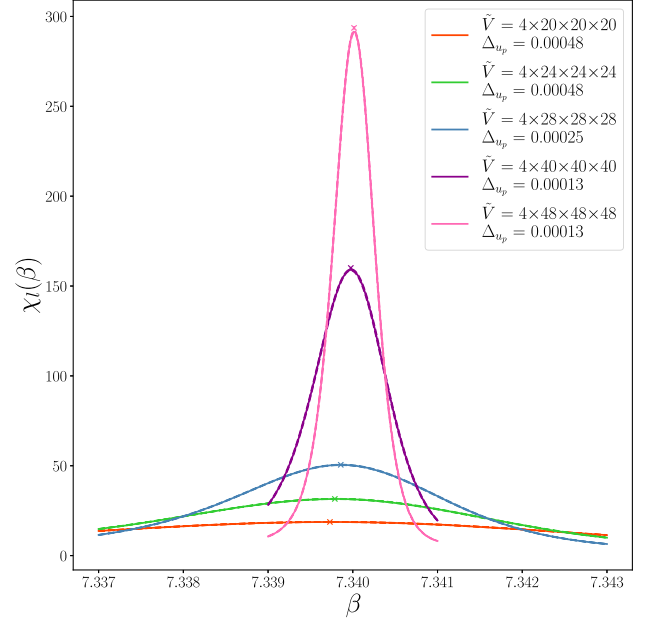

FIG. 10. The Polyakov loop susceptibility, $\chi_l(\beta)$, plotted as a function of coupling, β, for lattices with temporal size, $N_t = 4$, spatial sizes $N_s = 20, 24, 28, 40, 48$ (color coded), and subinterval sizes $\Delta_{u_p} = 0.00048, 0.00048, 0.00025, 0.00013, 0.00013$, respectively. We chose a grid with 100 evenly spaced values of β, in the interval $7.337 < \beta < 7.343$, for $N_s = 20, 24,$ and 28, and $7.339 < \beta < 7.341$ for $N_s = 40$ and 48.
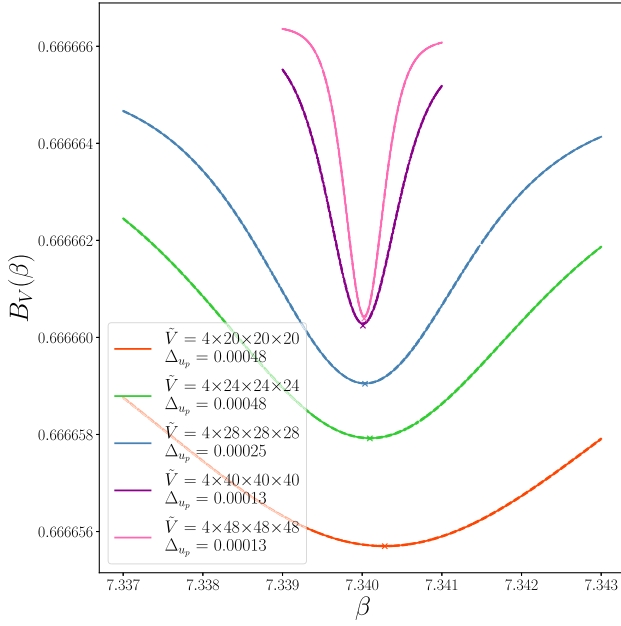
FIG. 11. The Binder cumulant, $B_V(\beta)$, plotted as a function of coupling, β, for lattices with temporal size, $N_t = 4$, spatial sizes $N_s = 20$, 24, 28, 40, 48 (color coded), and subinterval sizes $\Delta_{u_p} = 0.00048$, 0.00048, 0.00025, 0.00013, 0.00013, respectively. We chose a grid with 1000 evenly spaced values of β, in the interval $7.337 < \beta < 7.343$, for $N_s = 20$, 24, and 28, and $7.339 < \beta < 7.341$, for $N_s = 40$ and 48.

Another expectation of the thermodynamic limit, in the presence of first-order phase transitions, and based on the double Gaussian approximation, is that the peak of the specific heat, $C_V^{(\max)}$, should approach a value proportional to the square of the plaquette jump—see Eq. (23). In Fig. 13, we compare the square of the measured value of the plaquette jump, found directly from the plaquette distribution at the critical point, with the peak of the specific heat, for all spatial sizes. In both cases we take the limit of vanishing interval size, as discussed in Appendix D.

To test the theoretical expectation, we fit the specific heat term, $4a^4 C_V^{(\max)}/(6\tilde{V})$, to a quadratic polynomial in the cube of the inverse of the aspect ratio, N_t^3/N_s^3. We then extrapolate the fitting result to the limit $N_t/N_s \to 0$. The reduced chi-square of the fit is $\chi/N_{\mathrm{d.o.f.}}^2 = 5.5$. The extrapolation is $4a^4 C_V^{(\max)}/(6\tilde{V}) = 5.85(2)(1) \times 10^{-6}$. We also fit a function of the same form to the square of the plaquette discontinuity, $\Delta\langle u_p\rangle_{\beta_{CV}}^2$. The reduced chi-square is, in this case, $\chi^2/N_{\mathrm{d.o.f.}} = 0.18$ and the extrapolation is $\Delta\langle u_p\rangle_{\beta_C}^2 = 6.09(7) \times 10^{-6}$. These extrapolations do not agree, yet for the two largest volumes, $N_s = 40$ and 48, both observables are consistent. This could indicate that higher order effects of the scaling need to be considered to improve the fit process itself. Further measurements at additional values of N_s may be required, to verify if a
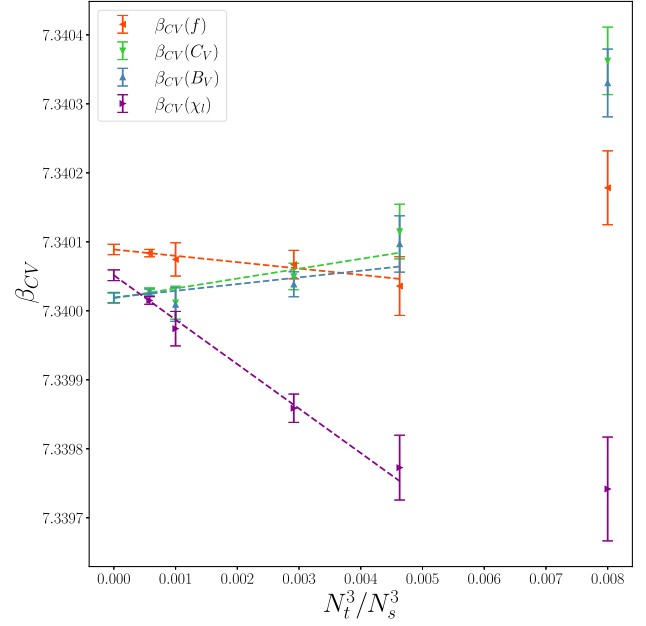

FIG. 12. Extrapolation towards the thermodynamic limit of the critical coupling defined in four alternative ways. The first definition is based on the crossing between the two metastable branches in the study of f, as displayed in Fig. 2, and denoted $\beta_{CV}(f)$. The other three definitions involve locating the extrema of the specific heat, $\beta_{CV}(C_V)$, the Binder cumulant, $\beta_{CV}(B_V)$, and the Polyakov loop susceptibility, $\beta_{CV}(\chi_l)$. We show the four measurements in different colors, for each available different volume, or the inverse of the aspect ratio N_t^3/N_s^3, at fixed temporal size, $N_t = 4$. The spatial sizes are $N_s = 20$, 24, 28, 40, 48. For each spatial volume, we use measurements extrapolated to the limit of vanishing interval size—see Appendix D. Linear fits of the four largest spatial sizes is shown by the dashed lines, and the extrapolations to the $N_s \to \infty$ are displayed at the left of the plot.

divergence between the observables grows, or if they do tend to the same value.

We conclude with two final measurements. First, the Polyakov loop susceptibility evaluated at criticality is expected to scale linearly with the volume. In Fig. 14, we plot the value of the peak of the Polyakov loop susceptibility normalized by the volume, $a^4 \chi_l^{(\max)}/\tilde{V}$, against the cube of the inverse of the aspect ratio. We fit a linear function in N_t^3/N_s^3 to the results for $N_s \geq 28$. We find a relatively large reduced chi-square $\chi^2/N_{\mathrm{d.o.f.}} = 6.7$. The extrapolation to the thermodynamic limit is given by $a^4 \chi_l^{(\max)}/\tilde{V} = 6.83(3)(5) \times 10^{-4}$.

In Fig. 15, we plot the value of the minimum of the Binder cumulant, $B_V^{(\min)}$, as a function of the cube of the inverse of the aspect ratio. We fit the measurements to a quadratic function in the cube of the inverse of the aspect ratio. The reduced chi-square for this fit is $\chi^2/N_{\mathrm{d.o.f.}} = 6.2$. The extrapolation to the limit $N_t/N_s \to 0$ is given by
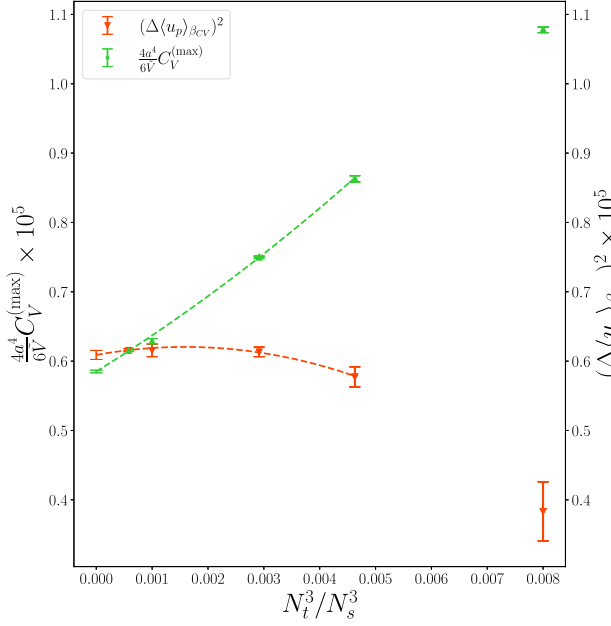
FIG. 13. The square of the plaquette discontinuity measured at the critical point, $(\Delta \langle u_p \rangle_{\beta_{CV}})^2$ (red), and the peak of the specific heat, normalized by the volume, $\frac{4a^4}{6V} C_V^{(\mathrm{max})}$ (green), as a function of the cube of the inverse of the aspect ratio, N_t^3/N_s^3. The two quantities as expected to agree in the thermodynamic limit—see Eq. (23). The lattices have temporal size $N_t = 4$, and spatial sizes $N_s = 20, 24, 28, 40, 48$. For each spatial volume we extrapolate to the limit of vanishing subinterval size—see Appendix D. The dashed lines show the results of quadratic polynomial fits of the four largest spatial volumes. The thermodynamic limits, $N_s \to \infty$, are displayed at the far left of the plot.

FIG. 14. Maxima of the Polyakov loop susceptibility, $\chi_l^{(\mathrm{max})}$, as a function of the cube of the inverse of the aspect ratio, N_t^3/N_s^3. The lattices considered have fixed temporal size, $N_t = 4$, and spatial sizes $N_s = 20, 24, 28, 40, 48$. For each spatial volume we use the extrapolations to the limit of vanishing subinterval size—see Appendix D. The black dashed curve shows a quadratic polynomial fit to the results for the three largest spatial volumes. The fit had reduced chi-square $\chi^2/N_{\mathrm{d.o.f.}} = 6.7$. The thermodynamic limit, $N_s \to \infty$, yields $a^4 \chi_l^{(\mathrm{max})}/\tilde{V} = 6.83(3)(5) \times 10^{-4}$, and is displayed at the far left of the plot.

$B_V^{(\mathrm{min})} = 0.66666069(2)(1)$. The value of $2/3$ (expected in second-order phase transitions) lies outside the error of this measurement. The reduced chi-square for this fit is large, as it might be affected by subleading corrections to the double-Gaussian approximation which arise from the mixed phase and the interface contributions.

While the statistical error on each or our measurements demonstrates the potential of the LLR algorithm to improve by several order of magnitude the precision of the measurements in the literature, however sizable systematic errors are present on the extrapolations to the thermodynamic limit. This can be seen by the comparably high reduced chi-square for the fits of the maximum of the specific heat, $C_V^{(\mathrm{max})}$, the minima of the Binder cumulant, $B_V^{(\mathrm{min})}$ and the maxima of the Polyakov loop susceptibility, $\chi_l^{(\mathrm{max})}$. It can also be seen from the disagreement between different extrapolations, for example in the relation between $C_V^{(\mathrm{max})}$ and the plaquette jump, and the different definitions of the critical couplings β_C. One possible explanation for these effects is that the double Gaussian approximation might be not accurate enough to describe
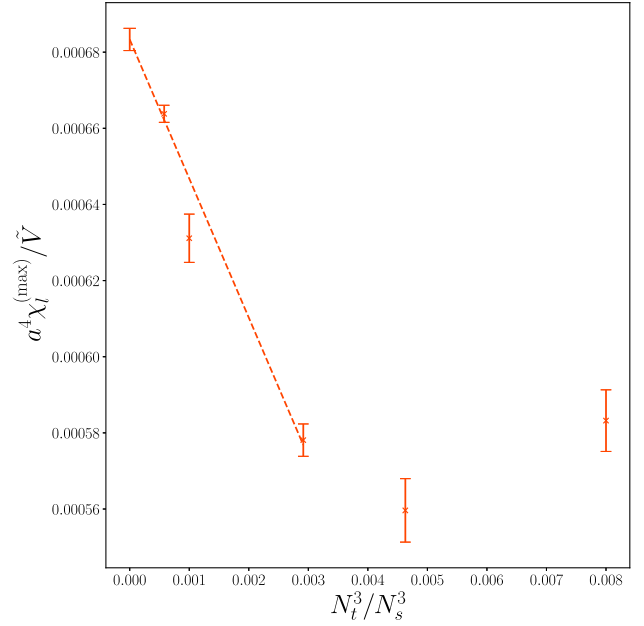
the scaling at larger volumes, as it ignores mixed phase configurations on the observables.

VI. OUTLOOK

We applied the LLR algorithm to perform our first extensive, high-statistics numerical study of the finite-temperature, confinement/deconfinement phase transition in the $Sp(4)$ lattice gauge theory. For each of the lattice volumes available, we measured the three main quantities that characterize the transition: the critical coupling, β_C, the discontinuity in the plaquette, $\Delta \langle u_p \rangle_{\beta_C}$, and the quantity, $\tilde{I}$, that in the thermodynamic limit yields the interface tension, $\lim_{\frac{N_t}{N_s} \to 0} \tilde{I} = \tilde{\sigma}_{cd}$.

The first step of our analysis was to apply the LLR algorithm to reconstruct the density of states of the theory. Having done so, we measured the free energy density, f. We demonstrated its multivalued nature, as expected in a first-order phase transition, in the region near criticality. We identified two competing metastable phases and one unstable mixed phase. We proceeded to compute other phenomenological observables, such as the probability distribution of the plaquette, the VEV of the average plaquette, the interphase contribution to the dynamics,
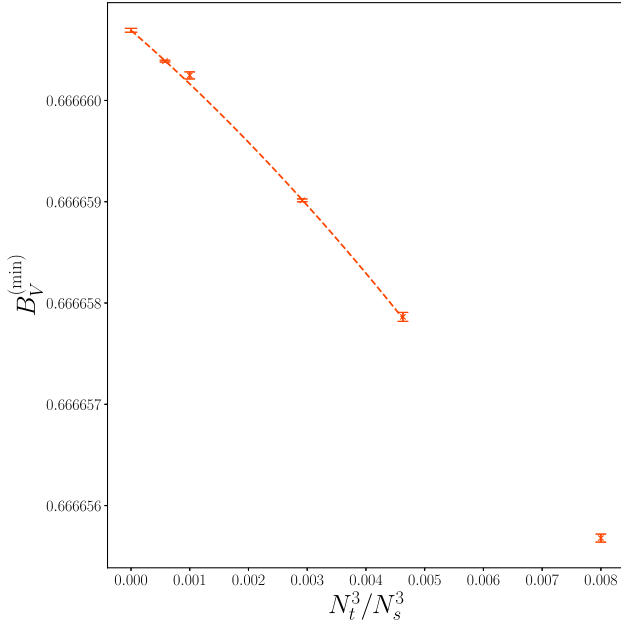
FIG. 15. Minima of the Binder cumulant, $B_V^{(\mathrm{min})}$, as a function of the cube of the inverse of the aspect ratio, N_t^3/N_s^3. The lattices considered have fixed temporal size, $N_t = 4$, and spatial sizes $N_s = 20, 24, 28, 40, 48$. For each spatial volume we use the extrapolations to the limit of vanishing subinterval size—see Appendix D. The black dashed curve shows a quadratic polynomial fit to the results for the four largest spatial volumes. The fit had reduced chi-square $\chi^2/N_{\mathrm{d.o.f.}} = 6.2$. The thermodynamic limit, $N_s \to \infty$, yields $0.66666069(2)(1)$, and is displayed at the far left of the plot.

the VEV of the absolute value of the Polyakov loop, as well as its susceptibility, and the Binder cumulant.

We performed our numerical studies on a number of lattices with different volumes. For each, we rerun the LLR algorithm with several different choices of the extent of the subinterval, Δu_p, used in defining the log-linear approximation, $\tilde{\rho}$, to the true density of states of the theory, ρ. We then performed two extrapolations. For each lattice volume, we combined all the measurements obtained with different extent of the subintervals, Δ_{u_p}, and extrapolated to the limit $\Delta u_p \to 0$, so that $\tilde{\rho} \to \rho$. We then considered the thermodynamic limit: holding fixed the temporal extent of the lattice, $N_t = 4$, we extrapolated all the measurements to the infinite volume limit in spatial extent, $N_s \to +\infty$.

We obtained four determinations of the critical coupling in the $Sp(4)$ lattice gauge theory, for $N_t = 4$, in $1 + 3$ dimensions, which we repeat here,

$$\beta_C(f) = 7.340089(8)(2),$$
$$\beta_C(C_V) = 7.340018(7)(5),$$
$$\beta_C(B_V) = 7.340019(7)(5),$$
$$\beta_C(\chi_l) = 7.340052(8)(4).$$

The labels of the four determinations refer to the different observables used in the extraction of the critical coupling. Our results are compatible with early measurement found in the literature, $\beta_C = 7.339(1)$ [133]. But the statistical error, which is obtained by repeating the LLR measurement with n_R replicas, and then bootstrapping the results, is 2 orders of magnitudes smaller than that quoted in the literature, which demonstrates the potential of the LLR method as a precision tool. We also measured, for $N_t = 4$, the infinite-volume extrapolations,

$$\lim_{N_t/N_s \to 0} \Delta \langle u_p \rangle_{\beta_C} = 0.002468(13)(1),$$
$$\lim_{N_t/N_s \to 0} \tilde{I} = 0.01718(32)(1).$$

These two quantities, discussed in the body of the paper, are related to latent heat and interface tension.

However, the flexibility and precision provided by the LLR algorithm also ended up exposing the presence of unknown systematics in the infinite-volume extrapolations. In particular, the four determinations of β_C are not compatible with one another, within statistical errors. The systematic uncertainty as estimated in this work (see Appendixes D and E) only partially addresses the discrepancy. Resolving the latter is then the first target of future high precision studies. We envision to use a combination of large volumes to gain better control on the approach to the thermodynamic limit, in the four observables of interest.

The next step requires to remove discretization effects, and extrapolate to the continuum limit. To this purpose, we envision repeating the same analysis, with different choices of N_t, and combine the results. At the time of writing this paper, we have started exploratory runs for $N_t = 5$—see some preliminary results in Appendix C. This program is going to be computationally challenging, as resolving the critical region near the transition for large choices of N_t requires performing the whole LLR study with increasingly large spatial volumes, N_s^3.

Our third goal for future investigation is quite ambitious. This whole analysis exposed here can be repeated for other theories. Our collaboration is particularly interested in the $SU(3)$ Yang-Mills theory [164–166], but other gauge groups are of interest as well [167–170], and it would be equally interesting to consider theories coupled to fermions, besides the Yang-Mills dynamics. These are challenging calculations, but the present study demonstrates that the LLR algorithm has the potential to lead to a revolutionary improvement in our control of the physics near the transition, which might have both theoretical and phenomenological implications, in particle as in astroparticle physics.

DATA AVAILABILITY

The data that support the findings of this article [204], the analysis workflow used to obtain them [204], and the software used to generate the underlying data analyzed [205] are openly available.

APPENDIX A: LLR ALGORITHM

The coefficients, a_n, defined in Eq. (10), are found by solving numerically, for each a_n, the equation,

$$0 = \langle\!\langle \Delta E \rangle\!\rangle_n(a_n)$$
$$= \frac{1}{\mathcal{N}_n(a_n)} \int_{E_n - \frac{\Delta_E}{2}}^{E_n + \frac{\Delta_E}{2}} dE (E - E_n)\rho(E)e^{-aE}, \quad \text{(A1)}$$

in each interval, $n = 1, \ldots, N_{\text{int}}$, with

$$\mathcal{N}_n(a_n) \equiv \int_{E_n - \frac{\Delta_E}{2}}^{E_n + \frac{\Delta_E}{2}} \rho(E)e^{-a_n E}dE. \quad \text{(A2)}$$

The double angle brackets denote the expectation value of an observable computed with energy restricted to an interval, $E_n - \Delta_E/2 < E < E_n + \Delta_E/2$. This interval differs from the interval in Eq. (10), to allow for an overlap region between adjacent intervals for replica exchange as we will discus shortly.

We solve this equation iteratively, by using a combination of Newton-Raphson (NR) and Robbins-Monro (RM) methods. We denote our approximations as $a_n^{(m)} \approx a_n$, where (m) is the iteration number. Each NR or RM update then takes this estimate and improves it, taking $a_n^{(m)} \to a_n^{(m+1)}$, having started from an initial trial value, $a_n^{(0)}$. The NR iteration is given by

$$a_n^{(m+1)} = a_n^{(m)} - \frac{12}{\Delta_E^2} \langle\!\langle \Delta E \rangle\!\rangle_n(a_n^{(m)}), \quad \text{(A3)}$$

while the RM method increments are finer, with

$$a_n^{(m+1)} = a_n^{(m)} - \frac{12}{(m+1)\Delta_E^2} \langle\!\langle \Delta E \rangle\!\rangle_n(a_n^{(m)}). \quad \text{(A4)}$$

The NR iterations bring the system close to the true value more quickly than the RM iteration, but the RM iteration are required to refine the accuracy of the estimate.

The double-angle-bracket expectation values are recalculated at each step, using configurations generated by a combination of over-relaxation and heat-bath steps, with energy restricted to the prescribed interval. The restricted heat-bath algorithm is discussed in Appendix A of Ref. [166], which we adapted to symplectic gauge groups,

as discussed in Appendix B. For each NR and RM iteration, we generate n_{Th} configurations to reduce autocorrelation, then measure $\langle\langle\Delta E\rangle\rangle_n(a)$ using n_M configurations. For lattices with $N_t = 4$, the values of the parameters n_{Th} and n_M are listed in Table I.

The lattice is decomposed into N_D subdomains. To account for the fact that the ensembles we produce are defined by a the global constraint on the energy, we perform a restricted heat-bath update on one subdomain at a time, chosen on a rota, while on the other subdomains we carry out an over-relaxation update. One full lattice update is complete when each subdomain has undergone one restricted heat-bath update.

To ensure ergodicity, we determine a_n in all intervals simultaneously, by running one independent lattice for each interval. Between each (NR or RM) iteration, we introduce the possibility of a swap between two lattices in adjacent intervals, if they are both in the shared overlap region. The swaps are stochastically determined, with probability,

$$P_{\mathrm{swap}} = \min\left(1, e^{(a_n^{(m)} - a_{n-1}^{(m)})(E_n^{(m)} - E_{n-1}^{(m)})}\right). \qquad (\text{A5})$$

Furthermore, we smoothen the sharp cutoffs in the distribution appearing at the end points of the total interval. We do so in the first (last) interval $E_1 - \Delta_E/2 < E < E_1 + \Delta_E/2$ (and $E_{N_{\mathrm{int}}} - \Delta_E/2 < E < E_{N_{\mathrm{int}}} + \Delta_E/2$), by replacing the boundaries with $0 < E < E_1 + \Delta_E/2$ (and $E_{N_{\mathrm{int}}} - \Delta_E/2 < E < 6\tilde{V}/a^4$). In this case the NR and RM iterations cannot be used. Instead, we assume that at the boundary a_n changes approximately linearly, making $a_1 \equiv 2a_2 - a_3$ and $a_{N_{\mathrm{int}}} \equiv 2a_{N_{\mathrm{int}}-1} - a_{N_{\mathrm{int}}-2}$.

As explained in the body of the paper, starting points, $a_n^{(0)}$, are determined through a rough preliminary calculation using important sampling methods. A systematic error is introduced by the truncation of the iterative process after $\bar{m}$ NR and $\tilde{m}$ RM iterations. We estimate its size by repeating our determination of a_n with a different random seed, and measuring the distribution of the results. As each replica begins in a randomly generated configuration, before we can use the action in constrained updates, the energy of the lattice system must be brought into the relevant interval. We refer to this process as annealing. This is achieved by using standard heat-bath updates with the coupling set to the initial value of a_n. After each update, we check if the energy is within the relevant interval, if it is we have finished annealing. After a set number of updates, if the system is still not within the interval, the coupling is changed—it is increased if $E < E_n$ and decreased if $E > E_n$.

Once the RM iterations have completed, our final values, $\{a_n^{(\tilde{m})} \approx a_n\}_{n=1}^{N_{\mathrm{int}}}$, have been determined for each interval centered at $\{E_n\}_{n=1}^{N_{\mathrm{int}}}$. We then carry out a set of restricted heat-bath updates. On each configuration, we measure the Polyakov loop and the average plaquette. To maintain ergodicity, after n_{fxa} iterations we apply a replica exchange,

and further repeat the process $\hat{m}$ times. This yields $n_{\mathrm{fxa}} \times \hat{m}$ measurements in each interval to estimate Eq. (16) for an arbitrary value of β. We hence arrive at the expectation value in Eq. (15). The error on this VEV is determined by bootstrapping over the results from each replica.

We conclude by providing a schematic description of the whole algorithm.

(A) Choose the energy range physically relevant to the problem, $[E_{\min}, E_{\max}]$, and divide it into N_{int} subintervals, with energies centered at $E_n = E_{\min} + n\Delta_E/2$, for $n = 1, \ldots, N_{\mathrm{int}}$. Define initial values, $a_n^{(0)}$, for each of the intervals.

(B) Repeat n_R times with different random sequences:
(1) Start replica in a random configuration and anneal. Then thermalise with action-constrained updates.
(2) Repeat $\bar{m}$ times:
   (a) Thermalize with n_{Th} action-constrained updates.
   (b) Measure $(E - E_n)$ on n_M action-constrained updates to calculate the VEV in Eq. (A3) and update a_n.
   (c) Consider configuration swaps using Eq. (A5).
(3) Repeat $\tilde{m}$ times:
   (a) Thermalize with n_{Th} action-constrained updates.
   (b) Measure E on n_M action-constrained updates to calculate the VEV in Eq. (A4) and update a_n.
   (c) Consider configuration swaps using Eq. (A5).
(4) Repeat $\hat{m}$ times:
   (a) Identify a_n with the final values, $a_n^{(\tilde{m})}$, generate n_{fxa} for configurations restricted to each interval and measure an observable $O[U]$ on them. In this work $O[U] = l_p[U]$.
   (b) Consider configuration swaps using Eq. (A5).

APPENDIX B: RESTRICTED HEAT-BATH ALGORITHM FOR $Sp(2N)$ GAUGE GROUPS

The link variables of the lattice are sampled following the prescription outlined in Ref. [206] and extended to $Sp(2N)$ gauge groups in Ref. [179]. The $Sp(2N)$ elements are generated by updating $SU(2) \sim Sp(2)$ subgroups, themselves sampled through energy-restricted heat-bath updates, as discussed in Appendix A of Ref. [166]. Given a link variable $U \in SU(2)$, and $U_{\sqcup}$ the staple around U, which has determinant k, the updated link is then given by $U' = UU_{\sqcup}/k$. In order to determine U, we use the standard $SU(2)$ parametrization of the nontrivial part of the embedding as $U = u_0 \mathbb{I}_2 + i\vec{u} \cdot \vec{\tau}$, where $\vec{\tau}$ are the Pauli matrices and $\mathbb{I}_2$ is the 2×2 identity matrix. We sample uniformly $\vec{u}$ from a sphere of radius $\sqrt{1 - u_0^2}$. Finally, u_0 is sampled by randomly generating a real variable, $0 \leq \xi \leq 1$, and defining

$$u_0 = \frac{1}{\beta k} \log\left(e^{-\beta k u_{\min}} + \xi(e^{\beta k u_{\max}} - e^{-\beta k u_{\min}})\right), \qquad (\text{B1})$$

where $u_{\min}$ and $u_{\max}$ are determined imposing the constraints $E_{n-1} \leq E - E_i + E_f \leq E_{n+1}$, where E is the total energy of

the original configuration, E_i is the contribution to E given by the old link and E_f is the energy contribution given by the new link.

The $SU(2)$ subgroups of $Sp(2N)$ can have two different structures. For instance, for $Sp(4)$ they can be either of the form,

$$\begin{pmatrix} u_0 + iu_3 & 0 & u_1 - iu_2 & 0 \\ 0 & 1 & 0 & 0 \\ -u_1 - iu_2 & 0 & u_0 - iu_3 & 0 \\ 0 & 0 & 0 & 1 \end{pmatrix}, \quad \text{(B2)}$$

or of the form,

$$\begin{pmatrix} u_0 + iu_3 & u_1 - iu_2 & 0 & 0 \\ -u_1 - iu_2 & u_0 - iu_3 & 0 & 0 \\ 0 & 0 & u_0 - iu_3 & u_1 + iu_2 \\ 0 & 0 & -u_1 + iu_2 & u_0 + iu_3 \end{pmatrix}. \quad \text{(B3)}$$

In both cases, we can write $E_f = 2(d-1) - kzu_0$, where z will change depending on the trace of the specific subgroup.[6] We then set $z = 1$ for the subgroups given in Eq. (B2) and $z = 2$ for the subgroups given in Eq. (B3). With these conventions, the constraints of u_0 become

$$u_{\min} = \max\left(\frac{2(d-1) + (E - E_{n+1}) - E_i}{kz}, -1\right), \quad \text{(B4)}$$

$$u_{\max} = \min\left(\frac{2(d-1) + (E - E_{n-1}) - E_i}{kz}, 1\right). \quad \text{(B5)}$$

One heat-bath sweep requires the sequential update of all links of the lattice using this procedure.

APPENDIX C: $N_t = 5$

While this paper focuses on the measurements in the $Sp(4)$ lattice gauge theory with lattices having fixed temporal extent, $N_t = 4$, yet, our long term objective is to extrapolate our measurements toward the continuum limit. We hence started exploratory runs to repeat our analysis for different values of N_t. In this appendix we present preliminary results for $N_t = 5$. Using standard importance sampling methods, we determined that a spatial size of $N_s = 40$ is the minimum one required to resolve the double peak structure in the plaquette distribution. We hence chose to perform our preliminary analysis with the spatial sizes $N_s = 48$ and $N_s = 56$.

We carried out an importance sampling analysis on $Sp(4)$ pure gauge theory with lattice size 5×48^3. We considered lattice couplings $\beta = 7.480, 7.490, 7.493,$

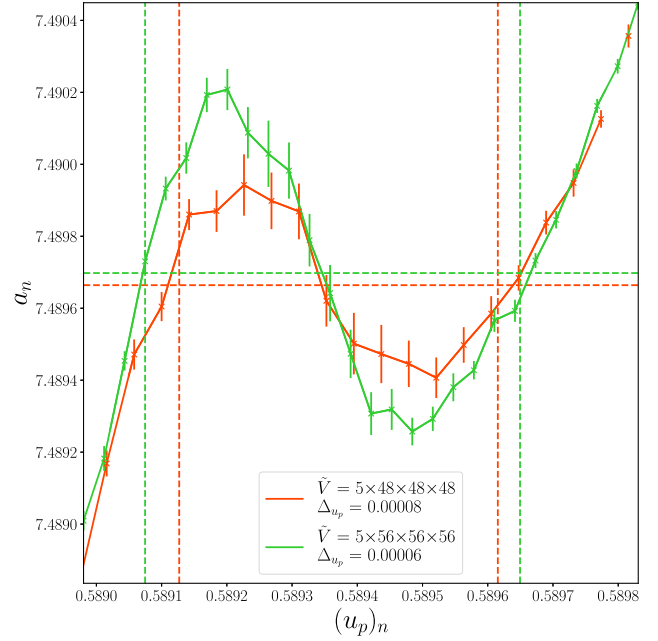[6]This formula also applies to $SU(N)$, for which $z = 1$.

FIG. 16. The coefficients a_n, plotted as a function of the plaquette value at the center of the energy interval, $(u_p)_n$, for the $Sp(4)$ theory on lattices with temporal size of $N_t = 5$, spatial sizes $N_s = 48, 56$, and plaquette subinterval sizes $\Delta_{u_p} = 0.00008$, and $\Delta_{u_p} = 0.00006$, respectively, shown in different colors. The plot is focused on the critical region, showing the characteristic noninvertible structure of $a_n((u_p)_n)$. The horizontal dashed lines show the critical coupling, $a_n = \beta_{CV}(f)$, and the vertical lines show the corresponding plaquette values.

7.495, and 7.4. For each update we carry out one heat-bath and four over-relaxation steps, and generated 10,000 configurations, after having disregarded 5000 thermalization steps. For each ensemble we measured the absolute value of the Polyakov loop and average plaquette. From the rough analysis of our results, we decided to fix the plaquette range of interest to be $(u_p)_{\min} = 0.5875 < u_p < (u_p)_{\max} = 0.5915$ and used a polinomyal fit of the plaquette to fix our initial estimates for the coefficients, $a_n^{(0)}$. Details on the LLR analysis are given in Table II.

Our measurement of the coefficients, a_n, determining the density of states are plotted against the plaquette value at the center of the interval, $(u_p)_n$, in Fig. 16. The plot focuses on the critical region, in which we find clear evidence of noninvertibility for the function $a_n(u_p)$. The horizontal dashed line shows the critical couplings relation to the coefficients, $a_n = \beta_{CV}(f)$, the vertical lines are the intercepts with the plaquette values, $u_p(a_n = \beta_{CV}(f))$ on the metastable branches. As for the case $N_t = 4$, we see that as the spatial volume grows, the range of a_n values in the noninvertible region grows, indicating that the range of β values that will be affected by metastable dynamics has grown. We notice that the value of the critical coupling is larger than for $N_t = 4$.
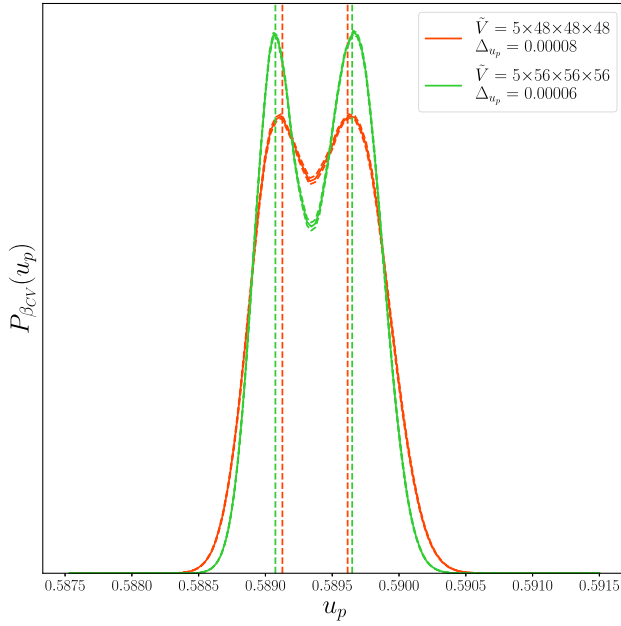
FIG. 17. The plaquette probability distribution, $P_\beta(u_p)$, in the $Sp(4)$ lattice gauge theory with $N_t = 5$, computed at the critical point, $\beta = \beta_{CV}(f)$. The plaquette distribution exhibits a double Gaussian structure with peaks of equal height. As in Fig. 16 the color coding represents two different spatial sizes, $N_s = 48$ and $N_s = 56$, with interval sizes $\Delta_{u_p} = 0.00008$ and $\Delta_{u_p} = 0.00006$ respectively. The horizontal dashed line shows the location of the peaks of the distribution. As the spatial volume is increases, the peaks become sharper.

But we also highlight that despite the large spatial value, the signal we detect is less pronounced. This is particularly clear when comparing the corresponding plaquette distributions, measured at the critical coupling, which are shown in Fig. 17. As we increase the spatial volume, the peaks become more pronounced, yet for these choices of volume the double Gaussian approximation is still accurate. We also show the reduced free-energy, $f(t)$, in Fig. 18, in which we subtracted the value at the point at which the two metastable branches cross, as for the $N_t = 4$ case. We conclude that the choices of spatial volume applied to this preliminary study are not close to the asymptotic regime, yet. Nevertheless, these measurements are sufficient to establish the first order nature of the transition, through both the double peak structure of the plaquette distribution and the swallow-tail structure of the free-energy.

In future work, we aim to extrapolate our analysis toward the continuum limit, which might be feasible if we are able to perform the thermodynamic limit on lattices with both $N_t = 5$ and $N_t = 6$. These are challenging goals, in view of the preliminary results shown here. In the $N_t = 4$, we only required an aspect ratio of around $N_s/N_t = 5$, to resolve the separate peaks at the critical point of the first order phase transition. For $N_t = 5$, we required an aspect ratio $N_s/N_t \sim 9.6$. An analysis of $N_t = 6$, therefore may require
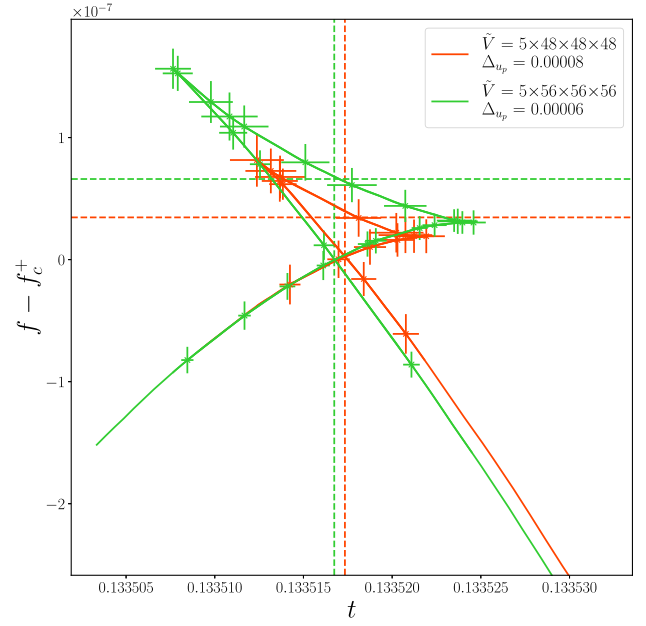

FIG. 18. The reduced free energy, f, a function of the microcanonical temperature, $t = 1/a_n$, for the $Sp(4)$ theory on lattices with temporal size $N_t = 5$, spatial sizes $N_s = 48$, and $N_s = 56$, and plaquette subinterval sizes $\Delta_{u_p} = 0.00008$, $\Delta_{u_p} = 0.00006$, respectively, as in Figs. 16 and 17. To ensure that the (reduced) free energy difference can be compared between different lattice sizes, constant term, f_c^+, has been subtracted, determined by the reduced free energy at which the two metastable branches cross.

further increases of the aspect ratio. Further software development on the parallelization of the algorithm may be required as well, before a satisfactory exploration of $N_t = 6$ case is feasible.

APPENDIX D: $\Delta_E \to 0$ LIMIT

Measurements obtained with the LLR method are affected by a systematic uncertainty related to the finite size of the subinterval in plaquette (or energy) of the system. One expects this effect to scale with the square of the interval size, Δ_E^2 [162]. In this appendix, we provide some additional details about the process we applied to accurately account for this source of uncertainty. For each of our measurements, we repeated the LLR process for multiple choice of subinterval sizes and took the limit $\Delta_E \to 0$ of the results.

We list in Tables III and IV the intermediate results used in the measurement of the relevant observables, as well as the resulting critical couplings. We report both the measurements obtained with finite choices of the plaquette subinterval, Δ_{u_p}, along with the extrapolations, $\Delta_{u_p} \to 0$. The uncertainties quoted for each finite subinterval size are calculated by bootstrapping the results for the n_R repeats. As explained elsewhere, we assume this estimate to capture in the stochastic error also the truncation error due to

TABLE III.   Measurements in the $Sp(4)$ pure gauge theory on lattices with temporal size $N_t = 4$, performed at the critical coupling, using the LLR algorithm, with subinterval size Δ_{u_p}. Extrapolations to the limit of vanishing subinterval size are denoted by $\Delta_{u_p} \to 0$. The final extrapolations to the thermodynamic limit are denoted by $N_s \to \infty$. We denote as $a^4 C_V^{(\mathrm{max})}/\tilde{V}$ and $a^4 \chi_l^{(\mathrm{max})}/\tilde{V}$ the extrema of the specific heat, C_V, and the Polyakov loop susceptibility, χ_l, scaled by the lattice volume $\tilde{V}/a^4$, respectively. The minima of the Binder cumulant are denoted as $B_V^{(\mathrm{min})}$. The plaquette discontinuity, $\Delta \langle u_p \rangle_{\beta_{CV}}$ is measured as the difference between the two peaks of the plaquette distribution, when the peaks are of equal height. The quantity $\hat{I}$ is defined in Eq. (29) and is related to the surface tension. For thermodynamic limit we include an additional bracket containing an estimation for the systematic error.

N_s	Δ_{u_p}	$a^4 C_V^{(\mathrm{max})}/\tilde{V}$	$B_V^{(\mathrm{min})}$	$a^4 \chi_l^{(\mathrm{max})}/\tilde{V}$	$\Delta \langle u_p \rangle_{\beta_{CV}}$	$\hat{I}$
20	0.00064	$1.611(3) \times 10^{-5}$	0.66665571(2)	$5.86(4) \times 10^{-4}$	0.002056(33)	0.03135(10)
20	0.00048	$1.614(2) \times 10^{-5}$	0.66665570(1)	$5.85(3) \times 10^{-4}$	0.002013(45)	0.03148(8)
20	$\to 0$	$1.617(6) \times 10^{-5}$	0.66665568(4)	$5.83(8) \times 10^{-4}$	0.001958(109)	0.03165(22)
24	0.00064	$1.280(2) \times 10^{-5}$	0.66665796(2)	$5.79(4) \times 10^{-4}$	0.002352(10)	0.02561(10)
24	0.00048	$1.286(3) \times 10^{-5}$	0.66665792(2)	$5.70(3) \times 10^{-4}$	0.002375(12)	0.02586(10)
24	$\to 0$	$1.294(7) \times 10^{-5}$	0.66665786(4)	$5.60(8) \times 10^{-4}$	0.002403(30)	0.02616(25)
28	0.00048	$1.109(2) \times 10^{-5}$	0.66665912(2)	$5.69(4) \times 10^{-4}$	0.002461(8)	0.02278(8)
28	0.00025	$1.120(1) \times 10^{-5}$	0.66665905(1)	$5.76(3) \times 10^{-4}$	0.002472(10)	0.02318(5)
28	$\to 0$	$1.125(2) \times 10^{-5}$	0.66665901(1)	$5.78(4) \times 10^{-4}$	0.002477(14)	0.02334(8)
40	0.00017	$0.944(2) \times 10^{-5}$	0.66666024(1)	$6.21(2) \times 10^{-4}$	0.002509(6)	0.01973(8)
40	0.00013	$0.944(2) \times 10^{-5}$	0.66666024(1)	$6.25(2) \times 10^{-4}$	0.002497(7)	0.01969(8)
40	$\to 0$	$0.943(5) \times 10^{-5}$	0.66666025(3)	$6.31(6) \times 10^{-4}$	0.002481(18)	0.01965(20)
48	0.00013	$0.922(1) \times 10^{-5}$	0.66666039(1)	$6.64(2) \times 10^{-4}$	0.002482(5)	0.01897(8)
$\to \infty$		$0.878(3)(1) \times 10^{-5}$	0.66666069(2)(1)	$6.83(3)(5) \times 10^{-4}$	0.002468(13)(1)	0.01718(32)(1)

TABLE IV.   Measurements of the critical coupling in the $Sp(4)$ pure gauge theory on lattices with temporal size $N_t = 4$, obtained with the LLR method. The plaquette subinterval size is denoted as Δ_{u_p}. Extrapolations to the limit of vanishing interval size are denoted by $\Delta_{u_p} \to 0$. The final extrapolations to the thermodynamic limit are denoted by $N_s \to \infty$. The coupling for which the free-energy on the metastable branches is equal is denoted as $\beta_{CV}(f)$, while $\beta_{CV}(C_V)$, $\beta_{CV}(B_V)$, and $\beta_{CV}(\chi_l)$, are the values of the couplings at the extrema of the specific heat, C_V, the Binder cumulant, B_V, and the Polyakov loop susceptibility, χ_l, respectively. For thermodynamic limit we include an additional bracket containing an estimation for the systematic error.

N_s	Δ_{u_p}	$\beta_{CV}(C_V)$	$\beta_{CV}(B_V)$	$\beta_{CV}(\chi_l)$	$\beta_{CV}(f)$
20	0.00064	7.340282(23)	7.340246(24)	7.339721(25)	7.340102(25)
20	0.00048	7.340317(17)	7.340283(17)	7.339730(30)	7.340136(19)
20	$\to 0$	7.340362(49)	7.340330(49)	7.339742(75)	7.340178(54)
24	0.00064	7.340111(19)	7.340095(19)	7.339800(20)	7.340058(20)
24	0.00048	7.340113(14)	7.340096(15)	7.339788(18)	7.340048(15)
24	$\to 0$	7.340115(40)	7.340097(41)	7.339773(47)	7.340036(43)
28	0.00048	7.340036(17)	7.340028(16)	7.339855(17)	7.340055(16)
28	0.00025	7.340046(13)	7.340035(12)	7.339858(14)	7.340064(14)
28	$\to 0$	7.340050(19)	7.340038(18)	7.339859(21)	7.340067(21)
40	0.00017	7.340011(9)	7.340009(8)	7.339978(8)	7.340079(9)
40	0.00013	7.340011(9)	7.340009(10)	7.339976(10)	7.340077(10)
40	$\to 0$	7.340012(24)	7.340009(24)	7.339974(25)	7.340074(24)
48	0.00013	7.340028(5)	7.340026(5)	7.340015(6)	7.340084(5)
$\to \infty$		7.340018(7)(5)	7.340019(7)(5)	7.340052(8)(4)	7.340089(8)(2)

carrying out a finite number of RM iterations. The extrapolations are calculated by taking the results for each lattice volume and performing a fit linear in the square of the interval size $\Delta_{u_p}^2$. The errors quote for the extrapolations are the fitting errors.

The extrapolation of the results in Δ_E^2 has a theoretical basis, see Ref. [162], and the scaling was demonstrated to be appropriate, for sufficiently small intervals, for the thermodynamic observables in the deconfinement transition in $SU(3)$ pure gauge theory, see Ref. [166]. We are

however, unable to verify this assumption in this case as we only have two interval sizes points per lattice volume. The requirement of an additional limit, $\Delta_E^2 \to 0$, is a drawback of the algorithm, with the cost of additional interval sizes being weighed against additional lattice volumes and lattice spacings. The focus of this work was to pursue the thermodynamic limit, and thus we opted to analyze two interval sizes per volume. Therefore, there is an additional systematic uncertainty, not quoted in the tables, due to taking the limit of vanishing interval size, which we estimate increases the total error by approximately 30%.

APPENDIX E: SYSTEMATIC UNCERTAINTY IN THE THERMODYNAMIC LIMIT

To estimate the systematic uncertainty on the infinite volume extrapolations due to our choice of parametrization, we use the Akaike information criterion (AIC), Ref. [207]. To each observable, we fit models with quadratic polynomials and linear polynomials, and exclude the smallest N_{cut} data points. For each model we calculate the AIC term, given in Eq. (161) in Ref. [208], and use this as a weight, $w_i \sim \exp(-\frac{1}{2}AIC)$. Further following the method presented in Sec. 21 of the Supplemental Information of Ref. [208], we estimate the combined extrapolation and total error by constructing a cumulative distribution function given by $\sum w_i N(\mu_i, \sigma_i)$, where $N(\mu_i, \sigma_i)$ is a Gaussian distribution centered on the result of each extrapolation, μ_i, with standard deviation given by the uncertainty on it, σ_i. From this we can get an estimate for the total error, including both stochastic and systematic sources, as the difference between the 16th and 84th percentile of the cumulative distribution, $\sigma_{\text{tot}} = \frac{1}{2}(y_{84} - y_{16})$. In the main body of the paper, Tables III and IV, we present the results and error for our choice of model, i^*, based on the AIC and other physical motivations, and additional the increase in error due to the systematics as, $\mu_{i^*}(\sigma_{i^*})(\sigma_{\text{tot}} - \sigma_i)$.

[1] A. D. Sakharov, Violation of *CP* Invariance, C asymmetry, and baryon asymmetry of the universe, Pis'ma Zh. Eksp. Teor. Fiz. **5**, 32 (1967).

[2] E. Witten, Cosmic separation of phases, Phys. Rev. D **30**, 272 (1984).

[3] M. Kamionkowski, A. Kosowsky, and M. S. Turner, Gravitational radiation from first order phase transitions, Phys. Rev. D **49**, 2837 (1994).

[4] B. Allen, The Stochastic gravity wave background: Sources and detection, in Les Houches School of Physics: Astrophysical Sources of Gravitational Radiation (1996), pp. 373–417, arXiv:gr-qc/9604033.

[5] P. Schwaller, Gravitational waves from a dark phase transition, Phys. Rev. Lett. **115**, 181101 (2015).

[6] D. Croon, V. Sanz, and G. White, Model discrimination in gravitational wave spectra from dark phase transitions, J. High Energy Phys. 08 (2018) 203.

[7] N. Christensen, Stochastic gravitational wave backgrounds, Rep. Prog. Phys. **82**, 016903 (2019).

[8] N. Seto, S. Kawamura, and T. Nakamura, Possibility of direct measurement of the acceleration of the universe using 0.1-Hz band laser interferometer gravitational wave antenna in space, Phys. Rev. Lett. **87**, 221103 (2001).

[9] S. Kawamura *et al.*, The Japanese space gravitational wave antenna DECIGO, Classical Quantum Gravity **23**, S125 (2006).

[10] J. Crowder and N. J. Cornish, Beyond LISA: Exploring future gravitational wave missions, Phys. Rev. D **72**, 083005 (2005).

[11] V. Corbin and N. J. Cornish, Detecting the cosmic gravitational wave background with the big bang observer, Classical Quantum Gravity **23**, 2435 (2006).

[12] G. M. Harry, P. Fritschel, D. A. Shaddock, W. Folkner, and E. S. Phinney, Laser interferometry for the big bang observer, Classical Quantum Gravity **23**, 4887 (2006); Classical Quantum Gravity **23**, 7361(E) (2006).

[13] S. Hild *et al.*, Sensitivity studies for third-generation gravitational wave observatories, Classical Quantum Gravity **28**, 094013 (2011).

[14] K. Yagi and N. Seto, Detector configuration of DECIGO/ BBO and identification of cosmological neutron-star binaries, Phys. Rev. D **83**, 044011 (2011); Phys. Rev. D **95**, 109901(E) (2017).

[15] B. Sathyaprakash *et al.*, Scientific objectives of Einstein telescope, Classical Quantum Gravity **29**, 124013 (2012); Classical Quantum Gravity **30**, 079501(E) (2013).

[16] E. Thrane and J. D. Romano, Sensitivity curves for searches for gravitational-wave backgrounds, Phys. Rev. D **88**, 124032 (2013).

[17] C. Caprini *et al.*, *Science* with the space-based interferometer eLISA. II: Gravitational waves from cosmological phase transitions, J. Cosmol. Astropart. Phys. 04 (2016) 001.

[18] P. Amaro-Seoane *et al.* (LISA Collaboration), Laser interferometer space antenna, arXiv:1702.00786.

[19] B. P. Abbott *et al.* (LIGO Scientific Collaboration), Exploring the sensitivity of next generation gravitational wave detectors, Classical Quantum Gravity **34**, 044001 (2017).

[20] S. Isoyama, H. Nakano, and T. Nakamura, Multiband gravitational-wave astronomy: Observing binary inspirals with a decihertz detector, B-DECIGO, Prog. Theor. Exp. Phys. **2018**, 073E01 (2018).

[21] J. Baker *et al.*, The laser interferometer space antenna: Unveiling the millihertz gravitational wave sky, arXiv:1907.06482.

[22] V. Brdar, A. J. Helmboldt, and J. Kubo, Gravitational waves from first-order phase transitions: LIGO as a window to unexplored seesaw scales, J. Cosmol. Astropart. Phys. 02 (2019) 021.

[23] D. Reitze *et al.*, Cosmic explorer: The U.S. contribution to gravitational-wave astronomy beyond LIGO, Bull. Am. Astron. Soc. **51**, 035 (2019).

[24] C. Caprini *et al.*, Detecting gravitational waves from cosmological phase transitions with LISA: An update, J. Cosmol. Astropart. Phys. 03 (2020) 024.

[25] M. Maggiore *et al.*, Science case for the Einstein telescope, J. Cosmol. Astropart. Phys. 03 (2020) 050.

[26] A. Afzal, G. Agazie, A. Anumarlapudi, A. M. Archibald, Z. Arzoumanian, P. T. Baker, B. Bécsy, J. J. Blanco-Pillado, L. Blecha, K. K. Boddy *et al.*, The nanograv 15 yr data set: Search for signals from new physics, Astrophys. J. Lett. **951**, L11 (2023).

[27] Y. Aoki, G. Endrodi, Z. Fodor, S. D. Katz, and K. K. Szabo, The order of the quantum chromodynamics transition predicted by the standard model of particle physics, Nature (London) **443**, 675 (2006).

[28] K. Kajantie, M. Laine, K. Rummukainen, and M. E. Shaposhnikov, Is there a hot electroweak phase transition at $m_H \gtrsim m_W$?, Phys. Rev. Lett. **77**, 2887 (1996).

[29] F. Karsch, T. Neuhaus, A. Patkos, and J. Rank, Critical Higgs mass and temperature dependence of gauge boson masses in the SU(2) gauge Higgs model, Nucl. Phys. B, Proc. Suppl. **53**, 623 (1997).

[30] M. Gurtler, E.-M. Ilgenfritz, and A. Schiller, Where the electroweak phase transition ends, Phys. Rev. D **56**, 3888 (1997).

[31] K. Rummukainen, M. Tsypin, K. Kajantie, M. Laine, and M. E. Shaposhnikov, The universality class of the electroweak theory, Nucl. Phys. **B532**, 283 (1998).

[32] F. Csikor, Z. Fodor, and J. Heitger, Endpoint of the hot electroweak phase transition, Phys. Rev. Lett. **82**, 21 (1999).

[33] Y. Aoki, F. Csikor, Z. Fodor, and A. Ukawa, The endpoint of the first order phase transition of the SU(2) gauge Higgs model on a four-dimensional isotropic lattice, Phys. Rev. D **60**, 013001 (1999).

[34] M. D'Onofrio and K. Rummukainen, Standard Model cross-over on the lattice, Phys. Rev. D **93**, 025003 (2016).

[35] M. Laine and K. Rummukainen, What's new with the electroweak phase transition?, Nucl. Phys. B, Proc. Suppl. **73**, 180 (1999).

[36] D. E. Morrissey and M. J. Ramsey-Musolf, Electroweak baryogenesis, New J. Phys. **14**, 125003 (2012).

[37] O. Gould, S. Güyer, and K. Rummukainen, First-order electroweak phase transitions: A nonperturbative update, Phys. Rev. D **106**, 114507 (2022).

[38] M. J. Strassler and K. M. Zurek, Echoes of a hidden valley at hadron colliders, Phys. Lett. B **651**, 374 (2007).

[39] K. Cheung and T.-C. Yuan, Hidden fermion as milli-charged dark matter in Stueckelberg Z′ model, J. High Energy Phys. 03 (2007) 120.

[40] T. Hambye, Hidden vector dark matter, J. High Energy Phys. 01 (2009) 028.

[41] J. L. Feng, M. Kaplinghat, H. Tu, and H.-B. Yu, Hidden charged dark matter, J. Cosmol. Astropart. Phys. 07 (2009) 004.

[42] T. Cohen, D. J. Phalen, A. Pierce, and K. M. Zurek, Asymmetric dark matter from a GeV hidden sector, Phys. Rev. D **82**, 056001 (2010).

[43] R. Foot and S. Vagnozzi, Dissipative hidden sector dark matter, Phys. Rev. D **91**, 023512 (2015).

[44] G. Bertone and D. Hooper, History of dark matter, Rev. Mod. Phys. **90**, 045002 (2018).

[45] M. Cirelli, A. Strumia, and J. Zupan, Dark matter, arXiv:2406.01705.

[46] E. Del Nobile, C. Kouvaris, and F. Sannino, Interfering composite asymmetric dark matter for DAMA and Co-GeNT, Phys. Rev. D **84**, 027301 (2011).

[47] A. Hietanen, R. Lewis, C. Pica, and F. Sannino, Composite Goldstone dark matter: Experimental predictions from the lattice, J. High Energy Phys. 12 (2014) 130.

[48] J. M. Cline, W. Huang, and G. D. Moore, Challenges for models with composite states, Phys. Rev. D **94**, 055029 (2016).

[49] G. D. Kribs and E. T. Neil, Review of strongly-coupled composite dark matter models and lattice simulations, Int. J. Mod. Phys. A **31**, 1643004 (2016).

[50] G. Cacciapaglia, C. Pica, and F. Sannino, Fundamental composite dynamics: A review, Phys. Rep. **877**, 1 (2020).

[51] N. A. Dondi, F. Sannino, and J. Smirnov, Thermal history of composite dark matter, Phys. Rev. D **101**, 103010 (2020).

[52] S. Ge, K. Lawson, and A. Zhitnitsky, Axion quark nugget dark matter model: Size distribution and survival pattern, Phys. Rev. D **99**, 116017 (2019).

[53] V. Beylin, M. Y. Khlopov, V. Kuksa, and N. Volchanskiy, Hadronic and hadron-like physics of dark matter, Symmetry **11**, 587 (2019).

[54] N. Yamanaka, H. Iida, A. Nakamura, and M. Wakayama, Dark matter scattering cross section and dynamics in dark Yang-Mills theory, Phys. Lett. B **813**, 136056 (2021).

[55] N. Yamanaka, H. Iida, A. Nakamura, and M. Wakayama, Glueball scattering cross section in lattice SU(2) Yang-Mills theory, Phys. Rev. D **102**, 054507 (2020).

[56] H. Cai and G. Cacciapaglia, Singlet dark matter in the SU (6)/SO(6) composite Higgs model, Phys. Rev. D **103**, 055002 (2021).

[57] Y. Hochberg, E. Kuflik, T. Volansky, and J. G. Wacker, Mechanism for thermal relic dark matter of strongly interacting massive particles, Phys. Rev. Lett. **113**, 171301 (2014).

[58] Y. Hochberg, E. Kuflik, H. Murayama, T. Volansky, and J. G. Wacker, Model for thermal relic dark matter of strongly interacting massive particles, Phys. Rev. Lett. **115**, 021301 (2015).

[59] Y. Hochberg, E. Kuflik, and H. Murayama, SIMP spectroscopy, J. High Energy Phys. 05 (2016) 090.

[60] N. Bernal, X. Chu, and J. Pradler, Simply split strongly interacting massive particles, Phys. Rev. D **95**, 115023 (2017).

[61] A. Berlin, N. Blinov, S. Gori, P. Schuster, and N. Toro, Cosmology and accelerator tests of strongly interacting dark matter, Phys. Rev. D **97,** 055033 (2018).

[62] N. Bernal, X. Chu, S. Kulkarni, and J. Pradler, Self-interacting dark matter without prejudice, Phys. Rev. D **101,** 055044 (2020).

[63] Y.-D. Tsai, R. McGehee, and H. Murayama, Resonant self-interacting dark matter from dark QCD, Phys. Rev. Lett. **128,** 172001 (2022).

[64] D. Kondo, R. McGehee, T. Melia, and H. Murayama, Linear sigma dark matter, J. High Energy Phys. 09 (2022) 041.

[65] X. Chu, M. Nikolic, and J. Pradler, Even SIMP miracles are possible, Phys. Rev. Lett. **133,** 021003 (2024).

[66] A. Maas and F. Zierler, Strong isospin breaking in $Sp(4)$ gauge theory, Proc. Sci. LATTICE2021 (**2022**) 130 [arXiv:2109.14377].

[67] F. Zierler and A. Maas, $Sp(4)$ SIMP dark matter on the lattice, Proc. Sci. LHCP2021 (**2021**) 162.

[68] S. Kulkarni, A. Maas, S. Mee, M. Nikolic, J. Pradler, and F. Zierler, Low-energy effective description of dark $Sp(4)$ theories, SciPost Phys. **14,** 044 (2023).

[69] J. Pomper and S. Kulkarni, Low energy effective theories of composite dark matter with real representations, arXiv:2402.04176.

[70] T. Appelquist, J. Ingoldby, and M. Piai, Dilaton forbidden dark matter, Phys. Rev. D **110,** 035013 (2024).

[71] T. Appelquist *et al.*, Stealth dark matter: Dark scalar baryons through the Higgs portal, Phys. Rev. D **92,** 075030 (2015).

[72] T. Appelquist *et al.*, Detecting stealth dark matter directly through electromagnetic polarizability, Phys. Rev. Lett. **115,** 171803 (2015).

[73] A. Francis, R. J. Hudspith, R. Lewis, and S. Tulin, Dark matter from strong dynamics: The minimal theory of dark baryons, J. High Energy Phys. 12 (2018) 118.

[74] V. I. Kalikmanov, *Nucleation Theory, Lecture Notes in Physics, Volume 860* (Springer Science+Business Media, Dordrecht, NL, 2013).

[75] W.-C. Huang, M. Reichert, F. Sannino, and Z.-W. Wang, Testing the dark SU(N) Yang-Mills theory confined landscape: From the lattice to gravitational waves, Phys. Rev. D **104,** 035005 (2021).

[76] J. Halverson, C. Long, A. Maiti, B. Nelson, and G. Salinas, Gravitational waves from dark Yang-Mills sectors, J. High Energy Phys. 05 (2021) 154.

[77] Z. Kang, J. Zhu, and S. Matsuzaki, Dark confinement-deconfinement phase transition: A roadmap from Polyakov loop models to gravitational waves, J. High Energy Phys. 09 (2021) 060.

[78] M. Reichert, F. Sannino, Z.-W. Wang, and C. Zhang, Dark confinement and chiral phase transitions: gravitational waves vs matter representations, J. High Energy Phys. 01 (2022) 003.

[79] M. Reichert and Z.-W. Wang, Gravitational waves from dark composite dynamics, EPJ Web Conf. **274,** 08003 (2022).

[80] R. Pasechnik, M. Reichert, F. Sannino, and Z.-W. Wang, Gravitational waves from composite dark sectors, J. High Energy Phys. 02 (2024) 159.

[81] R. D. Pisarski, Quark gluon plasma as a condensate of SU (3) Wilson lines, Phys. Rev. D **62,** 111501 (2000).

[82] R. D. Pisarski, Tests of the Polyakov loops model, Nucl. Phys. **A702,** 151 (2002).

[83] R. D. Pisarski, Notes on the deconfining phase transition, in *Cargese Summer School on QCD Perspectives on Hot and Dense Matter* (2002), pp. 353–384, arXiv:hep-ph/0203271.

[84] F. Sannino, Polyakov loops versus hadronic states, Phys. Rev. D **66,** 034013 (2002).

[85] C. Ratti, M. A. Thaler, and W. Weise, Phases of QCD: Lattice thermodynamics and a field theoretical model, Phys. Rev. D **73,** 014019 (2006).

[86] K. Fukushima and C. Sasaki, The phase diagram of nuclear and quark matter at high baryon density, Prog. Part. Nucl. Phys. **72,** 99 (2013).

[87] K. Fukushima and V. Skokov, Polyakov loop modeling for hot QCD, Prog. Part. Nucl. Phys. **96,** 154 (2017).

[88] P. M. Lo, B. Friman, O. Kaczmarek, K. Redlich, and C. Sasaki, Polyakov loop fluctuations in SU(3) lattice gauge theory and an effective gluon potential, Phys. Rev. D **88,** 074502 (2013).

[89] H. Hansen, R. Stiele, and P. Costa, Quark and Polyakov-loop correlations in effective models at zero and non-vanishing density, Phys. Rev. D **101,** 094001 (2020).

[90] P. N. Meisinger, T. R. Miller, and M. C. Ogilvie, Phenomenological equations of state for the quark gluon plasma, Phys. Rev. D **65,** 034009 (2002).

[91] A. Dumitru, Y. Guo, Y. Hidaka, C. P. K. Altes, and R. D. Pisarski, How wide is the transition to deconfinement?, Phys. Rev. D **83,** 034022 (2011).

[92] A. Dumitru, Y. Guo, Y. Hidaka, C. P. K. Altes, and R. D. Pisarski, Effective matrix model for deconfinement in pure gauge theories, Phys. Rev. D **86,** 105017 (2012).

[93] K.-I. Kondo, Confinement–deconfinement phase transition and gauge-invariant gluonic mass in Yang-Mills theory, arXiv:1508.02656.

[94] R. D. Pisarski and V. V. Skokov, Chiral matrix model of the semi-QGP in QCD, Phys. Rev. D **94,** 034015 (2016).

[95] H. Nishimura, R. D. Pisarski, and V. V. Skokov, Finite-temperature phase transitions of third and higher order in gauge theories at large N, Phys. Rev. D **97,** 036014 (2018).

[96] Y. Guo and Q. Du, Two-loop perturbative corrections to the constrained effective potential in thermal QCD, J. High Energy Phys. 05 (2019) 042.

[97] C. P. Korthals Altes, H. Nishimura, R. D. Pisarski, and V. V. Skokov, Free energy of a Holonomous Plasma, Phys. Rev. D **101,** 094025 (2020).

[98] Y. Hidaka and R. D. Pisarski, Effective models of a semi-quark-gluon plasma, Phys. Rev. D **104,** 074036 (2021).

[99] S. Borsanyi, R. Kara, Z. Fodor, D. A. Godzieba, P. Parotto, and D. Sexty, Precision study of the continuum SU(3) Yang-Mills theory: How to use parallel tempering to improve on supercritical slowing down for first order phase transitions, Phys. Rev. D **105,** 074513 (2022).

[100] G. Aarts *et al.*, Phase transitions in particle physics—results and perspectives from lattice quantum chromodynamics, Prog. Part. Nucl. Phys. **133,** 104070 (2023).

[101] B. Svetitsky and L. G. Yaffe, Critical behavior at finite temperature confinement transitions, Nucl. Phys. **B210,** 423 (1982).

[102] L. G. Yaffe and B. Svetitsky, First order phase transition in the SU(3) gauge theory at finite temperature, Phys. Rev. D **26,** 963 (1982).

[103] K. Kajantie, C. Montonen, and E. Pietarinen, Phase transition of SU(3) gauge theory at finite temperature, Z. Phys. C **9,** 253 (1981).

[104] T. Celik, J. Engels, and H. Satz, The order of the deconfinement transition in SU(3) Yang-Mills theory, Phys. Lett. B **125,** 411 (1983).

[105] J. B. Kogut, H. Matsuoka, M. Stone, H. W. Wyld, S. H. Shenker, J. Shigemitsu, and D. K. Sinclair, Quark and gluon latent heats at the deconfinement phase transition in SU(3) gauge theory, Phys. Rev. Lett. **51,** 869 (1983).

[106] B. Svetitsky and F. Fucito, Latent heat of the SU(3) gauge theory, Phys. Lett. **131B,** 165 (1983).

[107] S. A. Gottlieb, J. Kuti, D. Toussaint, A. D. Kennedy, S. Meyer, B. J. Pendleton, and R. L. Sugar, The deconfining phase transition and the continuum limit of lattice quantum chromodynamics, Phys. Rev. Lett. **55,** 1958 (1985).

[108] F. R. Brown, N. H. Christ, Y. F. Deng, M. S. Gao, and T. J. Woch, Nature of the deconfining phase transition in SU(3) lattice gauge theory, Phys. Rev. Lett. **61,** 2058 (1988).

[109] M. Fukugita, M. Okawa, and A. Ukawa, Order of the deconfining phase transition in SU(3) lattice gauge theory, Phys. Rev. Lett. **63,** 1768 (1989).

[110] P. Bacilieri *et al.*, A new computation of the correlation length near the deconfining transition in SU(3), Phys. Lett. B **224,** 333 (1989).

[111] N. A. Alves, B. A. Berg, and S. Sanielevici, Binder energy cumulant for SU(3) lattice gauge theory, Phys. Lett. B **241,** 557 (1990).

[112] G. Boyd, J. Engels, F. Karsch, E. Laermann, C. Legeland, M. Lutgemeier, and B. Petersson, Equation of state for the SU(3) gauge theory, Phys. Rev. Lett. **75,** 4169 (1995).

[113] G. Boyd, J. Engels, F. Karsch, E. Laermann, C. Legeland, M. Lutgemeier, and B. Petersson, Thermodynamics of SU(3) lattice gauge theory, Nucl. Phys. **B469,** 419 (1996).

[114] S. Borsanyi, G. Endrodi, Z. Fodor, S. D. Katz, and K. K. Szabo, Precision SU(3) lattice thermodynamics for a large temperature range, J. High Energy Phys. 07 (2012) 056.

[115] M. Shirogane, S. Ejiri, R. Iwami, K. Kanaya, and M. Kitazawa, Latent heat at the first order phase transition point of SU(3) gauge theory, Phys. Rev. D **94,** 014506 (2016).

[116] H. Saito, S. Ejiri, S. Aoki, T. Hatsuda, K. Kanaya, Y. Maezawa, H. Ohno, and T. Umeda (WHOT-QCD Collaboration), Phase structure of finite temperature QCD in the heavy quark region, Phys. Rev. D **84,** 054502 (2011); Phys. Rev. D **85,** 079902(E) (2012).

[117] S. Ejiri, S. Itagaki, R. Iwami, K. Kanaya, M. Kitazawa, A. Kiyohara, M. Shirogane, and T. Umeda (WHOT-QCD Collaboration), End point of the first-order phase transition of QCD in the heavy quark region by reweighting from quenched QCD, Phys. Rev. D **101,** 054505 (2020).

[118] A. Kiyohara, M. Kitazawa, S. Ejiri, and K. Kanaya, Finite-size scaling around the critical point in the heavy quark region of QCD, Phys. Rev. D **104,** 114509 (2021).

[119] M. Fromm, J. Langelage, S. Lottini, and O. Philipsen, The QCD deconfinement transition for heavy quarks and all baryon chemical potentials, J. High Energy Phys. 01 (2012) 042.

[120] F. Cuteri, O. Philipsen, A. Schön, and A. Sciarra, Deconfinement critical point of lattice QCD with $N_f = 2$ Wilson fermions, Phys. Rev. D **103,** 014513 (2021).

[121] S. Borsanyi, Z. Fodor, J. N. Guenther, R. Kara, P. Parotto, A. Pasztor, and D. Sexty, The upper right corner of the Columbia plot with staggered fermions, Proc. Sci. LATTICE2021 (**2022**) 496 [arXiv:2112.04192].

[122] B. Lucini, M. Teper, and U. Wenger, The deconfinement transition in SU(N) gauge theories, Phys. Lett. B **545,** 197 (2002).

[123] B. Lucini, M. Teper, and U. Wenger, The high temperature phase transition in SU(N) gauge theories, J. High Energy Phys. 01 (2004) 061.

[124] B. Lucini, M. Teper, and U. Wenger, Properties of the deconfining phase transition in SU(N) gauge theories, J. High Energy Phys. 02 (2005) 033.

[125] M. Panero, Thermodynamics of the QCD plasma and the large-N limit, Phys. Rev. Lett. **103,** 232001 (2009).

[126] S. Datta and S. Gupta, Continuum thermodynamics of the gluo N_c plasma, Phys. Rev. D **82,** 114505 (2010).

[127] B. Lucini, A. Rago, and E. Rinaldi, SU(N_c) gauge theories at deconfinement, Phys. Lett. B **712,** 279 (2012).

[128] M. Pepe, Confinement and the center of the gauge group, Proc. Sci. LAT2005 (**2006**) 017 [arXiv:hep-lat/0510013].

[129] M. Pepe and U. J. Wiese, Exceptional deconfinement in G (2) gauge theory, Nucl. Phys. **B768,** 21 (2007).

[130] G. Cossu, M. D'Elia, A. Di Giacomo, B. Lucini, and C. Pica, G_2 gauge theory at finite temperature, J. High Energy Phys. 10 (2007) 100.

[131] M. Bruno, M. Caselle, M. Panero, and R. Pellegrini, Exceptional thermodynamics: The equation of state of G_2 gauge theory, J. High Energy Phys. 03 (2015) 057.

[132] R. C. Brower *et al.* (Lattice Strong Dynamics Collaboration), Stealth dark matter confinement transition and gravitational waves, Phys. Rev. D **103,** 014505 (2021).

[133] K. Holland, M. Pepe, and U. J. Wiese, The deconfinement phase transition of Sp(2) and Sp(3) Yang-Mills theories in $(2 + 1)$-dimensions and $(3 + 1)$-dimensions, Nucl. Phys. **B694,** 35 (2004).

[134] M. Bruno, N. Forzano, M. Panero, and A. Smecca, Thermal evolution of dark matter in the early universe from a symplectic glueball model, arXiv:2410.17122.

[135] J. M. Maldacena, The large N limit of superconformal field theories and supergravity, Adv. Theor. Math. Phys. **2,** 231 (1998).

[136] S. S. Gubser, I. R. Klebanov, and A. M. Polyakov, Gauge theory correlators from noncritical string theory, Phys. Lett. B **428,** 105 (1998).

[137] E. Witten, Anti-de Sitter space and holography, Adv. Theor. Math. Phys. **2,** 253 (1998).

[138] O. Aharony, S. S. Gubser, J. M. Maldacena, H. Ooguri, and Y. Oz, Large N field theories, string theory and gravity, Phys. Rep. **323,** 183 (2000).

[139] E. Witten, Anti-de Sitter space, thermal phase transition, and confinement in gauge theories, Adv. Theor. Math. Phys. **2,** 505 (1998).

[140] I. R. Klebanov and M. J. Strassler, Supergravity and a confining gauge theory: Duality cascades and chi SB resolution of naked singularities, J. High Energy Phys. 08 (2000) 052.

[141] J. M. Maldacena and C. Nunez, Towards the large N limit of pure $N = 1$ superYang-Mills, Phys. Rev. Lett. **86,** 588 (2001).

[142] A. H. Chamseddine and M. S. Volkov, Non-Abelian BPS monopoles in $N = 4$ gauged supergravity, Phys. Rev. Lett. **79,** 3343 (1997).

[143] J. Babington, J. Erdmenger, N. J. Evans, Z. Guralnik, and I. Kirsch, Chiral symmetry breaking and pions in nonsupersymmetric gauge/gravity duals, Phys. Rev. D **69,** 066007 (2004).

[144] A. Butti, M. Grana, R. Minasian, M. Petrini, and A. Zaffaroni, The baryonic branch of Klebanov-Strassler solution: A supersymmetric family of SU(3) structure backgrounds, J. High Energy Phys. 03 (2005) 069.

[145] R. C. Brower, S. D. Mathur, and C.-I. Tan, Glueball spectrum for QCD from AdS supergravity duality, Nucl. Phys. **B587,** 249 (2000).

[146] A. Karch and E. Katz, Adding flavor to AdS/CFT, J. High Energy Phys. 06 (2002) 043.

[147] M. Kruczenski, D. Mateos, R. C. Myers, and D. J. Winters, Meson spectroscopy in AdS/CFT with flavor, J. High Energy Phys. 07 (2003) 049.

[148] T. Sakai and S. Sugimoto, Low energy hadron physics in holographic QCD, Prog. Theor. Phys. **113,** 843 (2005).

[149] T. Sakai and S. Sugimoto, More on a holographic dual of QCD, Prog. Theor. Phys. **114,** 1083 (2005).

[150] F. Bigazzi, A. Caddeo, A. L. Cotrone, and A. Paredes, Fate of false vacua in holographic first-order phase transitions, J. High Energy Phys. 12 (2020) 200.

[151] F. R. Ares, M. Hindmarsh, C. Hoyos, and N. Jokela, Gravitational waves from a holographic phase transition, J. High Energy Phys. 04 (2021) 100.

[152] Y. Bea, J. Casalderrey-Solana, T. Giannakopoulos, D. Mateos, M. Sanchez-Garitaonandia, and M. Zilhão, Bubble wall velocity from holography, Phys. Rev. D **104,** L121903 (2021).

[153] F. Bigazzi, A. Caddeo, T. Canneti, and A. L. Cotrone, Bubble wall velocity at strong coupling, J. High Energy Phys. 08 (2021) 090.

[154] O. Henriksson, Black brane evaporation through D-brane bubble nucleation, Phys. Rev. D **105,** L041901 (2022).

[155] F. R. Ares, O. Henriksson, M. Hindmarsh, C. Hoyos, and N. Jokela, Effective actions and bubble nucleation from holography, Phys. Rev. D **105,** 066020 (2022).

[156] F. R. Ares, O. Henriksson, M. Hindmarsh, C. Hoyos, and N. Jokela, Gravitational waves at strong coupling from an effective action, Phys. Rev. Lett. **128,** 131101 (2022).

[157] E. Morgante, N. Ramberg, and P. Schwaller, Gravitational waves from dark SU(3) Yang-Mills theory, Phys. Rev. D **107,** 036010 (2023).

[158] B. A. Berg and T. Neuhaus, Multicanonical algorithms for first order phase transitions, Phys. Lett. B **267,** 249 (1991).

[159] F. Wang and D. P. Landau, Efficient, multiple-range random walk algorithm to calculate the density of states, Phys. Rev. Lett. **86,** 2050 (2001).

[160] K. Langfeld, B. Lucini, and A. Rago, The density of states in gauge theories, Phys. Rev. Lett. **109,** 111601 (2012).

[161] K. Langfeld and J. M. Pawlowski, Two-color QCD with heavy quarks at finite densities, Phys. Rev. D **88,** 071502 (2013).

[162] K. Langfeld, B. Lucini, R. Pellegrini, and A. Rago, An efficient algorithm for numerical computations of continuous densities of states, Eur. Phys. J. C **76,** 306 (2016).

[163] G. Cossu, D. Lancastera, B. Lucini, R. Pellegrini, and A. Rago, Ergodic sampling of the topological charge using the density of states, Eur. Phys. J. C **81,** 375 (2021).

[164] D. Mason, B. Lucini, M. Piai, E. Rinaldi, and D. Vadacchino, The density of states method in Yang-Mills theories and first order phase transitions, EPJ Web Conf. **274,** 08007 (2022).

[165] D. Mason, B. Lucini, M. Piai, E. Rinaldi, and D. Vadacchino, The density of state method for first-order phase transitions in Yang-Mills theories, Proc. Sci. LAT-TICE2022 (**2023**) 216 [arXiv:2212.01074].

[166] B. Lucini, D. Mason, M. Piai, E. Rinaldi, and D. Vadacchino, First-order phase transitions in Yang-Mills theories and the density of state method, Phys. Rev. D **108,** 074517 (2023).

[167] F. Springer and D. Schaich, Density of states for gravitational waves, Proc. Sci. LATTICE2021 (**2022**) 043 [arXiv:2112.11868].

[168] F. Springer and D. Schaich, Progress applying density of states for gravitational waves, EPJ Web Conf. **274,** 08008 (2022).

[169] F. Springer and D. Schaich (Lattice Strong Dynamics (LSD) Collaboration), Advances in using density of states for large-N Yang–Mills, Proc. Sci. LATTICE2022 (**2023**) 223 [arXiv:2303.01149].

[170] F. Springer, D. Schaich, and E. Rinaldi (Lattice Strong Dynamics (LSD) Collaboration), First-order bulk transitions in large-N lattice Yang–Mills theories using the density of states, arXiv:2311.10243.

[171] J. Barnard, T. Gherghetta, and T. S. Ray, UV descriptions of composite Higgs models without elementary scalars, J. High Energy Phys. 02 (2014) 002.

[172] G. Ferretti and D. Karateev, Fermionic UV completions of composite Higgs models, J. High Energy Phys. 03 (2014) 077.

[173] G. Ferretti, Gauge theories of partial compositeness: Scenarios for Run-II of the LHC, J. High Energy Phys. 06 (2016) 107.

[174] G. Cacciapaglia, G. Ferretti, T. Flacke, and H. Serôdio, Light scalars in composite Higgs models, Front. Phys. **7,** 22 (2019).

[175] E. Bennett, D. K. Hong, J.-W. Lee, C. J. D. Lin, B. Lucini, M. Piai, and D. Vadacchino, Sp(4) gauge theory on the lattice: Towards SU(4)/Sp(4) composite Higgs (and beyond), J. High Energy Phys. 03 (2018) 185.

[176] E. Bennett, D. K. Hong, J.-W. Lee, C. J. D. Lin, B. Lucini, M. Piai, and D. Vadacchino, Sp(4) gauge theories on the lattice: $N_f = 2$ dynamical fundamental fermions, J. High Energy Phys. 12 (2019) 053.

[177] E. Bennett, D. K. Hong, J.-W. Lee, C.-J. D. Lin, B. Lucini, M. Mesiti, M. Piai, J. Rantaharju, and D. Vadacchino,

$Sp(4)$ gauge theories on the lattice: Quenched fundamental and antisymmetric fermions, Phys. Rev. D **101,** 074516 (2020).

[178] E. Bennett, J. Holligan, D. K. Hong, J.-W. Lee, C. J. D. Lin, B. Lucini, M. Piai, and D. Vadacchino, Color dependence of tensor and scalar glueball masses in Yang-Mills theories, Phys. Rev. D **102,** 011501 (2020).

[179] E. Bennett, J. Holligan, D. K. Hong, J.-W. Lee, C. J. D. Lin, B. Lucini, M. Piai, and D. Vadacchino, Glueballs and strings in $Sp(2N)$ Yang-Mills theories, Phys. Rev. D **103,** 054509 (2021).

[180] E. Bennett, D. K. Hong, H. Hsiao, J.-W. Lee, C. J. D. Lin, B. Lucini, M. Mesiti, M. Piai, and D. Vadacchino, Lattice studies of the Sp(4) gauge theory with two fundamental and three antisymmetric Dirac fermions, Phys. Rev. D **106,** 014501 (2022).

[181] E. Bennett, D. K. Hong, J.-W. Lee, C. J. D. Lin, B. Lucini, M. Piai, and D. Vadacchino, Color dependence of the topological susceptibility in Yang-Mills theories, Phys. Lett. B **835,** 137504 (2022).

[182] E. Bennett, D. K. Hong, J.-W. Lee, C. J. D. Lin, B. Lucini, M. Piai, and D. Vadacchino, Sp(2N) Yang-Mills theories on the lattice: Scale setting and topology, Phys. Rev. D **106,** 094503 (2022).

[183] E. Bennett, J. Holligan, D. K. Hong, H. Hsiao, J.-W. Lee, C. J. D. Lin, B. Lucini, M. Mesiti, M. Piai, and D. Vadacchino, Sp(2N) lattice gauge theories and extensions of the standard model of particle physics, Universe **9,** 236 (2023).

[184] E. Bennett et al., Symplectic lattice gauge theories in the grid framework: Approaching the conformal window, Phys. Rev. D **108,** 094508 (2023).

[185] E. Bennett, D. K. Hong, H. Hsiao, J.-W. Lee, C. J. D. Lin, B. Lucini, M. Piai, and D. Vadacchino, Lattice investigations of the chimera baryon spectrum in the Sp(4) gauge theory, Phys. Rev. D **109,** 094512 (2024).

[186] E. Bennett, J. Holligan, D. K. Hong, J.-W. Lee, C. J. D. Lin, B. Lucini, M. Piai, and D. Vadacchino, Spectrum of mesons in quenched Sp(2N) gauge theories, Phys. Rev. D **109,** 094517 (2024).

[187] E. Bennett et al., Meson spectroscopy from spectral densities in lattice gauge theories, Phys. Rev. D **110,** 074509 (2024).

[188] E. Bennett, N. Forzano, D. K. Hong, H. Hsiao, J.-W. Lee, C. J. D. Lin, B. Lucini, M. Piai, D. Vadacchino, and F. Zierler, Mixing between flavor singlets in lattice gauge theories coupled to matter fields in multiple representations, Phys. Rev. D **110,** 074504 (2024).

[189] J.-W. Lee, E. Bennett, D. K. Hong, C. J. D. Lin, B. Lucini, M. Piai, and D. Vadacchino, Progress in the lattice simulations of Sp(2N) gauge theories, Proc. Sci. LATTICE2018 (**2018**) 192 [arXiv:1811.00276].

[190] B. Lucini, E. Bennett, J. Holligan, D. K. Hong, H. Hsiao, J.-W. Lee, C. J. D. Lin, M. Mesiti, M. Piai, and D. Vadacchino, Sp(4) gauge theories and beyond the standard model physics, EPJ Web Conf. **258,** 08003 (2022).

[191] E. Bennett, J. Holligan, D. K. Hong, H. Hsiao, J.-W. Lee, C. J. D. Lin, B. Lucini, M. Mesiti, M. Piai, and

D. Vadacchino, Progress in $Sp(2N)$ lattice gauge theories, Proc. Sci. LATTICE2021 (**2022**) 308 [arXiv:2111.14544].

[192] H. Hsiao, E. Bennett, D. K. Hong, J.-W. Lee, C. J. D. Lin, B. Lucini, M. Piai, and D. Vadacchino, Spectroscopy of $Sp(4)$ lattice gauge theory with $n_f = 3$ antisymmetric fermions, Proc. Sci. LATTICE2022 (**2023**) 211 [arXiv:2210.08154].

[193] H. Hsiao, E. Bennett, D. K. Hong, J.-W. Lee, C. J. D. Lin, B. Lucini, M. Piai, and D. Vadacchino, Spectroscopy of chimera baryons in a $Sp(4)$ lattice gauge theory, arXiv:2211.03955.

[194] F. Zierler, J.-W. Lee, A. Maas, and F. Pressler, Singlet mesons in dark $Sp(4)$ theories, Proc. Sci. LATTICE2022 (**2023**) 225 [arXiv:2210.11187].

[195] F. Zierler, S. Kulkarni, A. Maas, S. Mee, M. Nikolic, and J. Pradler, Strongly interacting dark matter from Sp(4) gauge theory, EPJ Web Conf. **274,** 08014 (2022).

[196] E. Bennett, H. Hsiao, J.-W. Lee, B. Lucini, A. Maas, M. Piai, and F. Zierler, Singlets in gauge theories with fundamental matter, Phys. Rev. D **109,** 034504 (2024).

[197] Y. Dengler, A. Maas, and F. Zierler, Scattering of dark pions in an Sp(4)-gauge theory, Proc. Sci. LATTICE2023 (**2024**) 103 [arXiv:2311.18549].

[198] Y. Dengler, A. Maas, and F. Zierler, Scattering of dark pions in Sp(4) gauge theory, Phys. Rev. D **110,** 054513 (2024).

[199] D. Mason, B. Lucini, M. Piai, E. Rinaldi, and D. Vadacchino, The deconfinement phase transition in $Sp(2N)$ gauge theories and the density of states method, Proc. Sci. LATTICE2023 (**2024**) 085 [arXiv:2310.02145].

[200] B. A. Berg and T. Neuhaus, Multicanonical ensemble: A New approach to simulate first order phase transitions, Phys. Rev. Lett. **68,** 9 (1992).

[201] F. Karsch, SU(N) gauge theory couplings on asymmetric lattices, Nucl. Phys. **B205,** 285 (1982).

[202] M. S. S. Challa, D. P. Landau, and K. Binder, Finite size effects at temperature driven first order transitions, Phys. Rev. B **34,** 1841 (1986).

[203] G. V. Bhanot and S. Sanielevici, The BCL cumulant and lattice gauge theories: The order of the deconfinement transition, Phys. Rev. D **40,** 3454 (1989).

[204] E. Bennett, B. Lucini, D. Mason, M. Piai, E. Rinaldi, and D. Vadacchino, The density of states method for Symplectic gauge theories at finite temperature—data and analysis code release (2024), 10.5281/zenodo.13807598.

[205] E. Bennett, B. Lucini, D. Mason, M. Piai, E. Rinaldi, and D. Vadacchino, The density of states method for Symplectic gauge theories at finite temperature—HiRep LLR Code v1.0.0 (2024), 10.5281/zenodo.13807993.

[206] N. Cabibbo and E. Marinari, A new method for updating SU(N) matrices in computer simulations of gauge theories, Phys. Lett. **119B,** 387 (1982).

[207] H. Akaike, A new look at the statistical model identification, IEEE Trans. Autom. Control **19,** 716 (1974).

[208] S. Borsanyi et al., Leading hadronic contribution to the muon magnetic moment from lattice QCD, Nature (London) **593,** 51 (2021).